IAEA nuclear fusion

Flat-top plasma operational space of the STEP power plant

To cite this article: E. Tholerus *et al* 2024 *Nucl. Fusion* **64** 106030

OPEN ACCESS
IOP Publishing | International Atomic Energy Agency Nuclear Fusion

Nucl. Fusion **64** (2024) 106030 (32pp) https://doi.org/10.1088/1741-4326/ad6ea2

Flat-top plasma operational space of the STEP power plant

E. Tholerus[1,*], **F.J. Casson**[1], **S.P. Marsden**[1], **T. Wilson**[1], **D. Brunetti**[1], **P. Fox**[1], **S.J. Freethy**[1], **T.C. Hender**[1], **S.S. Henderson**[1], **A. Hudoba**[1], **K.K. Kirov**[1], **F. Koechl**[2], **H. Meyer**[1], **S.I. Muldrew**[1], **C. Olde**[1], **B.S. Patel**[1], **C.M. Roach**[1], **S. Saarelma**[1], **G. Xia**[1] **and the STEP team**[1]

[1] UKAEA (United Kingdom Atomic Energy Authority), Culham Campus, Abingdon, Oxfordshire OX14 3DB, United Kingdom of Great Britain and Northern Ireland
[2] ITER Organization, Route de Vinon-sur-Verdon, CS 90 046, 13067 St. Paul Lez Durance Cedex, France

E-mail: emmi.tholerus@ukaea.uk

Received 13 March 2024, revised 18 July 2024
Accepted for publication 13 August 2024
Published 30 August 2024

Abstract

STEP is a spherical tokamak prototype power plant that is being designed to demonstrate net electric power. The design phase involves the exploitation of plasma models to optimise fusion performance subject to satisfying various physics and engineering constraints. A modelling workflow, including integrated core plasma modelling, MHD stability analysis, SOL and pedestal modelling, coil set and free boundary equilibrium solvers, and whole plant design, has been developed to specify the design parameters and to develop viable scenarios. The integrated core plasma model JETTO is used to develop individual flat-top operating points that satisfy imposed criteria for fusion power performance within operational constraints. Key plasma parameters such as normalised beta, Greenwald density fraction, auxiliary power and radiated power have been scanned to scope the operational space and to derive a collection of candidate non-inductive flat-top points. The assumed auxiliary heating and current drive is either from electron cyclotron (EC) systems only or a combination of EC and electron Bernstein waves. At present stages of transport modelling, there is a large uncertainty in overall confinement for relevant parameter regimes. For each of the two auxiliary heating and current drive systems scenarios, two candidate flat-top points have been developed based on different confinement assumptions, totalling to four operating points. A lower confinement assumption generally suggests operating points in high-density, high auxiliary power regimes, whereas higher confinement would allow access to a broader parameter regime in density and power while maintaining target fusion power performance.

Keywords: STEP, integrated modelling, flat-top, JINTRAC, spherical tokamak

(Some figures may appear in colour only in the online journal)

---

[*] Author to whom any correspondence should be addressed.

1. Introduction

1.1. The spherical tokamak (ST) concept

Spherical Tokamak for Energy Production (STEP) is a DEMO-class [1] fusion experiment, intended to demonstrate net electricity production using the ST concept, with start of operation targeting 2040 [2–4]. The main feature that distinguishes STs from conventional tokamaks is the small aspect ratio, which maximises the relative extent of regions with favourable curvature along closed magnetic field lines. This allows for operation at higher β while avoiding pressure driven MHD instabilities such as ballooning modes. Thus, lower magnetic field strength can be used for the same kinetic pressure compared to conventional tokamaks. In addition, the lower aspect ratio also increases the natural elongation of the plasma [5]. As the bootstrap current fraction increases with both (poloidal) β and elongation [6, 7], less power is required for current drive in STs, improving the fusion Q for a steady-state device. Conventional tokamaks require large sizes and magnetic field strengths to reach reactor relevant confinement times, largely because of the expected negative β scaling of the confinement time when expressed in dimensionless 'physics' parameters [8, 9]. However, experiments on STs such as NSTX and MAST have indicated a weak negative or even positive scaling of energy confinement with respect to β [10], which would allow access to reactor relevant conditions at much smaller major radii, assuming that the suggested scaling laws extrapolate to these regimes.

The weaker magnetic field, lower power, and potentially smaller sizes required for reactor relevant conditions could make STs a generally more cost effective alternative to conventional tokamaks for commercial fusion power with steady state, non-inductive operation. However, the compact size leads to significant engineering challenges, particularly in the central column. The narrow central columns required by STs could limit the location of heating and fuelling systems mostly to the outer (low-field) side of the vessel. It also sets an upper limit to currents in the toroidal field coils and the central solenoid, which have to be sufficiently protected from radiation and mechanical stress. The more compact design relative to conventional tokamaks also puts higher requirements on the power load handling for the divertor and other plasma facing components. Exhaust is already one of the major technological challenges for conventional tokamak reactors.

1.2. STEP design parameters

STEP intends to demonstrate a net steady-state electric power output of at least 100 MW, corresponding to an engineering fusion energy gain factor $Q_{\mathrm{eng}} = P_{\mathrm{out}}/P_{\mathrm{in}}$ just above 1.0 (P_{out} is the gross electrical output, whereas P_{in} is the electrical power required to drive core systems and auxiliary heating during steady-state operation). The main design parameters planned for the presently envisaged STEP design are summarised in table 1, compared alongside other DEMO-class ST concepts suggested in the past. Here, R_{geo} is evaluated at the geometric centre of the mid-plane ($R_{\mathrm{geo}} = (R_{\mathrm{max}} + R_{\mathrm{min}})/2$), the aspect ratio $A = R_{\mathrm{geo}}/a_{\mathrm{min}}$ ($a_{\mathrm{min}} = (R_{\mathrm{max}} - R_{\mathrm{min}})/2$), κ_{95} is evaluated at the normalised poloidal flux $\psi_{\mathrm{N}} = 0.95$, and B_{geo} is the vacuum toroidal magnetic field evaluated at $R = R_{\mathrm{geo}}$. Section 2 presents motivations for the presented design parameters mainly from a core plasma performance perspective. Additional considerations in the chosen design have been outlined in [4, 11].

Comparing to the previously suggested DEMO-class ST concepts in table 1, STEP is both the largest, with $R_{\mathrm{geo}} = 3.6\,\mathrm{m}$, it has the highest toroidal field, with $B_{\mathrm{geo}} = 3.2\,\mathrm{T}$, and it has the lowest confinement factor, with $H_{\mathrm{IPB98(y,2)}} = 1.03$. The aspect ratio is also in the higher end, with $A = 1.8$. It should be noted that a number of different STEP flat-top scenarios are considered, as presented in section 5, which all have different sets of pros and cons in terms of performance and viability (the specific STEP scenario in table 1 is referred to as 'EB-CC' in this paper). Some of the concepts use auxiliary heating and current drive from Electron Cyclotron (EC) systems only, i.e. without Electron Bernstein Waves (EBWs). All ST concepts in table 1 utilise non-inductive current drive, and a high elongation $\kappa \sim 3$ to maximise the bootstrap current fraction. STEP is the only concept that does not use neutral beam injection (NBI) for heating and current drive. Although NBI has a relatively high current drive efficiency, it has been excluded for engineering reasons, e.g. requiring high acceleration voltage > 1 MV, and a large port size that reduces the tritium breeding volume (see details in [14]).

The confinement factor compares the energy confinement time against an empirical scaling (in this case the ITER H-mode scaling $\tau_{\mathrm{IPB98(y,2)}}$ [8]). A low value ($H_{\mathrm{IPB98(y,2)}} \lesssim 1$) provides confidence to the confinement assumption, since that has been more commonly demonstrated in experiments. This is also where STEP stands out compared to other DEMO-class ST concepts, with $H_{\mathrm{IPB98(y,2)}} \approx 1$. However, when discussing the specifics of the confinement assumptions for STEP in section 2.6, a modified estimate of the confinement factor is used that takes a fraction of the radiation losses into account [15]. This increases the confinement factor to values no lower than 1.19.

STEP will be fitted with tritium breeding blankets on the low-field side for regeneration of tritium fuel and for protection of sensitive components, such as superconducting field coils, from 14 MeV neutrons. The total fusion power P_{fus} during flat-top operation aims for a range of 1.5–1.8 GW. A calculation example of the full steady-state power cycle for STEP, including estimated electrical power requirements for core systems, wall-plug efficiencies of auxiliary heating and current drive systems, power losses in all stages of the cycle, and heat to electricity conversion efficiency, demonstrates that a scientific fusion energy gain factor $Q_{\mathrm{sci}} \gtrsim 11$ ($Q_{\mathrm{sci}} = P_{\mathrm{fus}}/P_{\mathrm{aux}}$ where P_{fus} is the total fusion power, and P_{aux} is the auxiliary heating power injected into the plasma) is consistent with a net electricity output $P_{\mathrm{net,elec.}} = P_{\mathrm{out}} - P_{\mathrm{in}} > 100\,\mathrm{MW}$ [4]. However, there are large uncertainties in the specific power requirements, efficiencies and losses in present stages of the STEP design, meaning that the recommended limit $Q_{\mathrm{sci}} \gtrsim 11$ might change with later designs. Further details on the limits for fusion power performance are given in section 2.2.

Table 1. Main machine parameters for a set of suggested DEMO-class ST experiments. EC stands for electron cyclotron systems, EBW is electron Bernstein waves, and NBI is neutral beam injection.

Parameter	STEP	ST DEMO [12]	STPP [6]	BurST [13]
Major radius, R_{geo} [m]	3.6	3.2	3.42	2.5
Aspect ratio, A [ ]	1.8	1.7	1.4	1.67
Elongation, κ	3.0 (κ_{95} : 2.8)	3.3	3.2	2.8
Toroidal field, B_{geo} [T]	3.2	2.4	1.77	2.4
Fusion power, P_{fus} [GW]	1.56	2.29	3.1	1.1
Plasma current, I_{p} [MA]	22.7	26.2	31	21.0
Conf. factor, $H_{\mathrm{IPB98(y,2)}}$	1.03	1.23	1.6	1.4
Auxiliary power	EC+EBW	NBI	NBI/EC(+EBW)	NBI

The central column has a diameter close to 3.0 m. In order to provide space for superconducting toroidal field coils sufficiently protected from radiation and mechanical stress, only a low-capacity central solenoid can be fitted ($I_{\mathrm{ind}} \sim 2\,\mathrm{MA}$), which is used for assisting start-up of scenarios only. Flat-top operation is fully non-inductive, with current driven by a combination of auxiliary systems and the bootstrap current. Two different auxiliary heating and current drive scenario options are being assessed for the current machine design. The first option includes microwave heating and current drive with both EC and EBW systems. Since the theory and modelling of EBW has less experimental validation compared to EC, a second option that includes EC systems only is being developed. These methods for auxiliary heating and current drive in STEP have been suggested after careful consideration of alternative methods [14]. Although both EC, EBW and fusion alphas primarily heat electrons, sufficient ion temperatures are still expected due to low ion heat diffusivity and heat flux predicted by gyrokinetic modelling [16–19] and experience from ST experiments [20]. Furthermore, for larger device sizes, the confinement time is expected to increase relative to the energy exchange time, in effect leading to equilibration of electron and ion temperatures [21].

Exhaust management is one of the major challenges of reactor relevant STs. The currently suggested design of the STEP divertor is double null [22–25]. Precise control of the separation between the two separatrices is required for sufficient distribution of the power loads between the divertors. To minimise erosion, mitigate particle flux, and buffer small transients in power, a detached plasma is needed during all main stages of operation (ramp-up, flat-top and ramp-down), which in turn requires high divertor neutral pressure, high radiation, and low $P_{\mathrm{sep}}/R_{\mathrm{geo}}$ [26, 27]. High neutral pressure is accessed by puffing D_2 and T_2 gas[3] from the divertor regions together with divertor design and tuning of the pumping speed, whereas low $P_{\mathrm{sep}}/R_{\mathrm{geo}}$ is achieved by enhancing the core radiation up to 70% of the total heating power using xenon-doped pellets. The STEP divertor also includes additional design features, such as a radially extended outer leg, and an inner leg that approaches an X-divertor magnetic geometry. These features help to increase the poloidal flux expansion and the connection length, which contributes both to an increased operational space for detachment access and to overall reduced heat loads. The materials of the high heat flux handling components remain to be confirmed, with some potential options being tungsten or tungsten alloys, or alternatively liquid tin armour.

1.3. Integrated modelling workflow

The integrated modelling workflow for developing flat-top operation points is shown in figure 1. The presented workflow is part of a larger scale iterative design process for developing more detailed engineering specifications, full scenarios including ramp-up and ramp-down, and assessments concerning e.g. cost, lifetime, environmental impact and safety of the whole scientific project [4]. Several potential concepts have been developed with 0.5D systems code PROCESS [28–30]. The 1.5D integrated core plasma model JETTO [31] has then been used to analyse the viability of each concept from a core plasma perspective. Additional codes for MHD stability (MISHKA [32–35] and MARS [36]), free boundary equilibrium solving (Fiesta [37]), heating & current drive modelling (GRAY [38], GENRAY [39] and CQL3D [40]), and pedestal modelling (Europed [41]) are iterated against JETTO solutions to further test viability of scenarios and to gradually refine modelling assumptions against detailed physics and engineering considerations. In the final step of the flat-top modelling workflow, the concept is further analysed with gyrokinetic codes (GS2 [42], CGYRO [43] and GENE [44]) to verify transport assumptions, and scrape-off layer modelling (SOLPS-ITER [45]) to study exhaust challenges.

This paper primarily presents the JETTO part of the modelling workflow used to guide the definition of the STEP operational space during flat-top. The way JETTO has been run in the presented modelling is referred to as ‘assumption integration’ mode, which means that confinement is assumed rather than predicted by first-principle transport models. An empirical transport model is used to define the profile shape of the heat and particle transport coefficients. An overall scaling factor on the diffusivities are then adjusted in a feedback loop to match a target value for the total (termal + fast) normalised beta β_{N} while keeping the relative electron to ion heat diffusivity ratio at a fixed level indicated by results from gyrokinetic modelling. The level of confinement that results from the

---

[3] While it is not impossible to design a fuel cycle that can maintain target D/T ratio with D_2 puffing only, the added complexity and cost to such a system makes the inclusion of T_2 gas preferable.

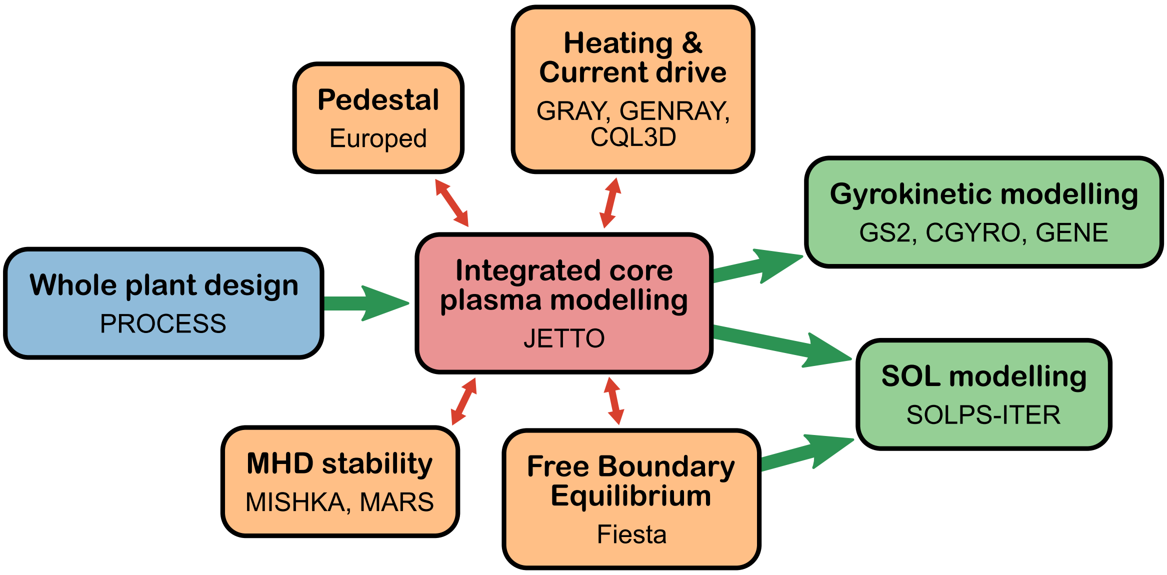

Figure 1. Diagram showing the stages of the workflow for developing flat-top operation points.

rescaling of the transport has to be assessed separately comparing to e.g. empirical confinement scalings. More details on the 'assumption integration' mode for JETTO is presented in section 3.3. As theoretical understanding of transport in STEP relevant regimes (i.e. high β, low collisionality, low torque and primarily electron heating) increases, JETTO modelling will transition to fully predictive transport and confinement.

The flat-top operational space is explored by performing a set of scans in key plasma parameters, with each scan point compared against operational limits that are motivated by performance requirements, engineering limitations and viability of modelling assumptions. The motivation for each of the considered operational limits in the parameter scans are presented in section 2. The specifics of JETTO and the assumptions used in the presented modelling are given in section 3. The section also presents the two reference JETTO simulations, with each scan using one of these references as a starting point. The reference simulations, referred to as 'scan templates', are either based on EC auxiliary heating and current drive only, or a combination of EC and EBW. Section 4 presents and discusses the results of the parameter scans. For each of the two auxiliary heating and current drive system scenarios, two candidate flat-top points have been developed based on different confinement assumptions. A higher acceptable level of confinement allows access to a broader operational space in density, temperature and auxiliary power. Two of the candidate operating points exploit these broadened parameter spaces, whereas the other two use more strict confinement assumptions. The four candidate operation points are presented in section 5. They have a higher degree of self-consistency compared to the simulations of the scans, including prediction of impurity density and radiation from transport and atomic physics, and q-profiles optimised for MHD stability. Finally, section 6 outlines the main conclusions.

2. Assumptions and constraints for the STEP flat-top

2.1. Geometry and magnetic field

The fusion power per unit volume of a magnetically confined D-T plasma scales as $P_{\mathrm{fus}}/V \propto n^2\langle\sigma v\rangle$ (any species indices are dropped in these derivations, assuming that $n_{\mathrm{D}} = n_{\mathrm{T}} = 0.5n_{\mathrm{e}}$ and $T_{\mathrm{i}} = T_{\mathrm{e}}$ for simplicity). For ion temperatures in the range 8–30 keV, the reactivity $\langle\sigma v\rangle \sim T^2$ [46], yielding $P_{\mathrm{fus}}/V \propto p^2 \propto \beta^2B^4$. Furthermore, it can be shown that $\beta \propto \beta_{\mathrm{N}}^2(1+\kappa^2)/(f_{\mathrm{BS}}\sqrt{A})$, based on the assumptions that $f_{\mathrm{BS}} \propto a^2p(1+\kappa^2)/(I_{\mathrm{p}}^2\sqrt{A}) \propto (aB/I_{\mathrm{p}})^2\beta(1+\kappa^2)/\sqrt{A}$ [47], and $aB/I_{\mathrm{p}} = \beta_{\mathrm{N}}/\beta$. This results in $P_{\mathrm{fus}}/V \propto \beta_{\mathrm{N}}^4B^4(1+\kappa^2)^2/(Af_{\mathrm{BS}}^2)$. For a ST, it can be assumed that the elongation $\kappa^2 \gg 1$, and the bootstrap current fraction $f_{\mathrm{BS}} \sim 1$. In these limits, the fusion power per unit volume scales as $P_{\mathrm{fus}}/V \propto (\beta_{\mathrm{N}}B\kappa)^4/A$. Multiplying by the volume $V \propto R_{\mathrm{geo}}^3\kappa/A^2$ yields the total fusion power $P_{\mathrm{fus}} \propto \beta_{\mathrm{N}}^4B^4\kappa^5R_{\mathrm{geo}}^3/A^3$, meaning that a high normalised beta, large major radius, high elongation, strong magnetic field, and low aspect ratio are all highly beneficial for fusion power performance.

The destabilisation of resistive wall modes (RWMs) sets an upper limit to β_{N}, which is discussed in more detail in section 2.4. Depending on the length of the confinement time, different levels of auxiliary heating and current drive are required to maintain the target β_{N}, which means that the fusion Q might be too low in case the confinement is poor. This is also an aspect to take into account when setting the target β_{N}. The elongation is limited by vertical stability constraints, although a lower internal inductance can increase the maximum elongation for vertical stability to some extent, with $\kappa_{\mathrm{max}} \sim 3.4 - l_{\mathrm{i}}$ [46]. The magnetic field strength is primarily constrained by regimes for efficient auxiliary heating and

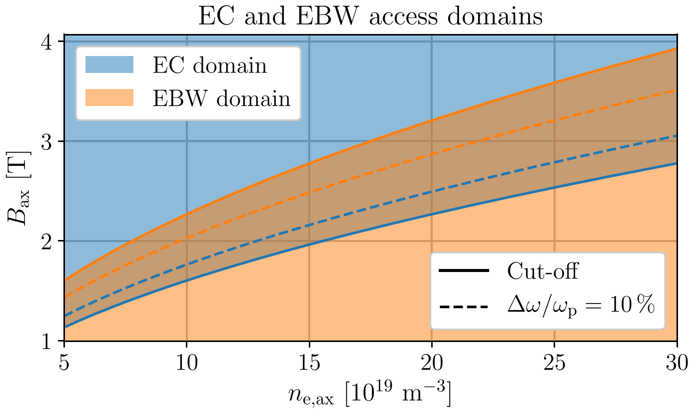

Figure 2. Approximate domains in $n_{e,ax}$,B_{ax}-space (subscript 'ax' corresponds to the value at the magnetic axis) with access to EC 2nd harmonic O-mode and EBW fundamental lower X-mode. Solid curves show the corresponding cut-off boundaries, and dashed lines show the boundaries at 10% frequency separation of the electron cyclotron frequency times the harmonic order relative to the plasma frequency. Details are given in section 2.3.

current drive schemes, with a narrow range where both 2nd harmonic O-mode (EC) and the fundamental lower X-mode (EBW) are accessible (see figure 2). Further details are given in section 2.3. The lower limit of the aspect ratio is primarily set by the required width of the central column to accommodate toroidal field coils and a low-capacity solenoid, sufficiently shielded from particle and electromagnetic radiation. Superconducting field coils are required to reach the target toroidal field without excessive power losses due to conductor resistivity. The main limitation for the major radius is cost. An overall larger major radius can help reduce the requirements on other parameters, e.g. β_N, elongation and aspect ratio, at maintained fusion power performance. However, with the restriction on the magnetic field for EC and EBW access, the rod current has to grow proportionally with the major radius, meaning that the central column needs to grow with increased capacity requirement of the toroidal field coils. Balancing the major radius against performance and cost, the presently suggested design point is at $R_{geo} = 3.6$ m. This choice is further motivated in [4]. The width requirement on the central column at that size suggests a minor radius of 2.0 m, i.e. an aspect ratio $A = 1.8$.

2.2. Fusion power and fusion Q

As already mentioned in section 1, the target fusion power is in the range 1.5–1.8 GW, with a $Q_{sci} > 11$. Even in the case of optimal Q_{sci}, where alpha heating alone is sufficient to maintain thermonuclear ion temperatures and auxilliary systems operate at minimal power for shaping the current profile, at least 1.5 GW of fusion power might be required to balance power requirements from systems such as field coils and cooling, considering the expected efficiency of energy conversion systems from the energetic neutrons to electric power. A fusion power of 1.8 GW corresponds to a neutron production rate of 6.4×10^{20} s^{-1}, and to an average power flux of 2.7 MW m^{-2} carried by neutrons as they cross the separatrix. Assuming for simplicity that all fusion reactions originate from the magnetic axis, the local power flux carried by neutrons would be around 5 MW m^{-2} on the first wall at the outer mid-plane.

For sufficient protection of all coil systems from the neutron flux, the coils need to be separated far enough from the first wall to allow space for tritium breeding blankets and other shielding components. This can become a challenge for control coils for RWM suppression (see details in section 2.4), which also need to be sufficiently close to the plasma to minimise the delay time of the field penetration in order to react to plasma conditions in real time. For an earlier STEP design, efficient control coil systems with a separation from the first wall have been demonstrated [48], which in principle should allow for breeding blankets to be installed between the coils and the plasma also in the updated STEP design.

2.3. EC and EBW access

Models for EC heating and current drive have been validated against several experiments, and the underlying theory is well understood. This contrasts to the lower level of maturity for EBW heating and current drive prediction. However, EBW remains a promising candidate for non-inductive current drive, due to the expected efficiency of power deposition to the high-energy tail of the electron distribution. In addition, a large Ohkawa current is predicted with the high trapped electron fraction in ST regimes [49, 50], which potentially makes EBW current drive significantly more efficient than ECCD for STEP. Two scenarios are being considered in parallel using EC heating and current drive only and using a combination of EC and EBW. The EC only scenario is modelled with a higher degree of confidence, due to the extensive validation of EC heating and current drive models against experiments, whereas simulations of the EC+EBW scenario suggest a more efficient power plant, requiring lower recirculation power [4].

ECCD has poor off-axis current drive efficiency due to the large trapped electron fraction. It is used in both STEP scenarios for on-axis auxiliary current drive, which is required to prevent current hole formation, with the bootstrap current vanishing on-axis (motivation for why on-axis current holes should be avoided is outlined in section 2.4). On the other hand, EBW is predicted to have low current drive efficiency on-axis, since the Doppler shift of the cyclotron harmonics causes all power to be deposited off-axis ($\rho_{\mathrm{tor}} \gtrsim 0.5$) before propagating to the core. Scans have been conducted in injector locations, steering mirror angles, and beam frequencies during STEP flat-top operation [51], using GRAY [38] benchmarked against CQL3D [40] for EC modelling, and GENRAY [39]/CQL3D for EBW modelling. It was shown that optimal ECCD efficiency is obtained by coupling to the 2$^{\mathrm{nd}}$ harmonic O-mode, with frequencies ranging between 130 and 200 GHz. EBW heating and current drive were shown to be the most feasible by access to the fundamental X-mode via conversion from O-mode, at frequencies 90–100 GHz. The X-mode wave then naturally transforms to a Bernstein wave (so called O-X-B coupling [52]).

A simple access criterion for EC heating and current drive is that the density cut-off is not exceeded on-axis, where the density is expected to be the highest. For the m^{th} harmonic O-mode, this criterion is

$$\omega_{\mathrm{c,e,ax}} > \frac{\omega_{\mathrm{p,ax}}}{m} \Leftrightarrow B_{\mathrm{ax}} > \sqrt{\frac{n_{\mathrm{e,ax}} m_{\mathrm{e}}}{m^2 \epsilon_0}}, \tag{1}$$

which corresponds to the blue domain in figure 2 for $m = 2$. This simple access criterion does not include effects, like harmonic shadowing, that arise from variation of density and magnetic field across the plasma. Nevertheless, it gives an indication of EC access that can be used for analysing the operational domains within the parameter scans in section 4.

A corresponding criterion can be formulated for EBW access. When the right hand cut-off frequency exceeds the frequency of the launched X-mode, a cut-off and the adjacent upper hybrid layers are guaranteed to exist in the plasma. The latter becomes the mode conversion layer for conversion into the EBW wave if warm plasma effects are accounted for. For an arbitrary harmonic $m \geqslant 1$, the criterion for the cut-off frequency to exceed the X-mode frequency can be formulated as

$$\begin{aligned} &\frac{1}{2}\left(\sqrt{\omega_{\mathrm{c,e,ax}}^2 + 4\omega_{\mathrm{p,ax}}^2} - \omega_{\mathrm{c,e,ax}}\right) > m\omega_{\mathrm{c,e,ax}} \\ &\Leftrightarrow \omega_{\mathrm{c,e,ax}} < \frac{\omega_{\mathrm{p,ax}}}{\sqrt{m(m+1)}}. \end{aligned} \tag{2}$$

Evaluated at $m = 1$ for the fundamental resonance, the inequality of equation (2) corresponds to the orange domain in figure 2.

2.4. MHD instabilities and q-profile shaping

Important MHD instabilities to consider in a ST include ballooning instabilities, sawteeth, neoclassical tearing modes (NTMs), RWMs, Alfvén eigenmodes (AEs), and edge-localised modes (ELMs). Many MHD instabilities can be avoided by strategic shaping of the q-profile. On-axis current hole formation with an associated strongly reversed shear q-profile should generally be avoided, since it can result in internal transport barriers that lead to disruptions [53]. Disruption events can be catastrophic at the plasma currents foreseen for STEP (see details in section 2.5). Strongly reversed q-profiles also risk destabilisation of double tearing modes [54, 55] and other mixed modes [56], and it can destabilise AEs [57, 58]. Non-inductive, high bootstrap current experiments such as STEP are vulnerable to current hole formation, since the bootstrap current density vanishes on-axis (the pressure gradient vanishes on-axis, and the bootstrap current contribution from potato orbits is expected to be negligible [59]), and there is no inductive current to fill the resulting gap. Thus, on-axis auxiliary current drive, e.g. from ECCD, is essential to complement the bootstrap current and to avoid the onset of a current hole.

The current density should be sufficiently low to avoid current driven MHD instabilities, such as sawteeth and low order NTMs occuring at $q = 2$ (which are likely to cause disruptions). Thus, q_{min} should be at least 2, which is consistent with direct access to second ballooning mode stability [60]. For NTMs, the strong curvature stabilisation at low aspect ratio [61] compared to the destabilising bootstrap term gives stability to $n = 1$ and $n = 2$ instabilities. In the shaping of the ECCD profile, the aim has been to achieve a relatively broad region around the axis ($\rho_{\mathrm{tor}} \lesssim 0.4$) with a low core magnetic shear out to $q \sim 3$. Since the equilibria tend to have low shear in the core, it is found that q_{min} above about 2.2 is necessary to avoid infernal modes [62] being unstable, or close to unstable, and coupling to RWMs. Tools have been developed for q-profile optimisation with ECCD shaping in STEP scenarios based on a genetic algorithm [63] and multi-objective Bayesian optimisation [64].

There is an upper limit of β_{N} (β_{N} includes both thermal and fast particle pressure, e.g. from alpha particles) for the destabilisation of RWMs, which grow on time scales similar to the vertical field diffusion time, a.k.a. the wall time. The degree of destabilisation can be quantified by the parameter

$$C_\beta = \frac{\beta_{\mathrm{N}} - \beta_{\mathrm{N}}^{\mathrm{no-wall}}}{\beta_{\mathrm{N}}^{\mathrm{ideal-wall}} - \beta_{\mathrm{N}}^{\mathrm{no-wall}}}, \tag{3}$$

where $\beta_{\mathrm{N}}^{\mathrm{no-wall}}$ and $\beta_{\mathrm{N}}^{\mathrm{ideal-wall}}$ are the RWM stability limits without and with a perfectly conducting wall, respectively. Operation at $C_\beta \gtrsim 1$, i.e. $\beta_{\mathrm{N}} \gtrsim \beta_{\mathrm{N}}^{\mathrm{ideal-wall}}$, will result in uncontrollable growth of RWMs. On the other hand, at domains of weakly positive C_β, with $\beta_{\mathrm{N}} \approx \beta_{\mathrm{N}}^{\mathrm{no-wall}}$, RWMs are likely to be stabilised by passive stabilisation mechanisms, such as plasma rotation [65] or kinetic resonances. At slightly higher $C_\beta \lesssim 0.5$, RWMs can be actively mitigated using control coils. Equation (3) considers destabilisation of the $n = 1$ toroidal mode, which typically has the lowest ideal-wall limit and is the most likely RWM to trigger disruption events. Multiple toroidal mode numbers are potentially destabilised at β_{N} above the corresponding no-wall limits, and need to be considered in the design of the active RWM mitigation systems.

Experiments have shown that the upper β_{N} limit can be expressed as a function of the pressure peaking $F_p = p_{\mathrm{ax}}/\langle p\rangle$ according to $\beta_{\mathrm{N}}^{\mathrm{ideal-wall}} = 0.2 + 12.5/F_p$ [66]. Assuming that this corresponds to the $n = 1$ ideal-wall limit, $C_\beta = 1$ matches this parametrisation. Simulations with the MHD code MARS-F [36] have shown that the no-wall limit is more or less independent of the pressure peaking, with a value close to 3.7 for STEP-like flat-tops. In the scans of section 4, an approximation of the destabilisation parameter

$$C_\beta \approx \frac{(\beta_\mathrm{N} - 3.7)\,F_p}{12.5 - 3.5F_p} \tag{4}$$

has been evaluated at each scan point based on the above assumptions, with an operational regime estimated as $C_\beta \leqslant 0.5$. This limit should only be interpreted as indicative of RWM stability, since there is additional physics that influences no-wall and ideal-wall β_N limits, which is not captured by the simple relationship of equation (4). The candidate flat-top points presented in section 5 have been further analysed with MARS-F to get a more accurate prediction of C_β.

Regarding stabilisation of RWMs by rotation, STEP does not have NBI systems, which would otherwise be the primary source of toroidal momentum. Although the alpha particles are born isotropic, particle losses during slowing down induce a net torque ($\boldsymbol{J} \times \boldsymbol{B}$-driven and collisional) [67], which can be enhanced by toroidal field ripple and the resonant magnetic perturbations from control coils [68]. Since the momentum diffusivity is not known for STEP relevant regimes, there are large uncertainties in the expected rotation resulting from the induced alpha particle torque. Consequently, rotation has not been included in our current JETTO calculations.

The Greenwald density $n_\mathrm{GW}[10^{20}\,\mathrm{m}^{-3}] = I_\mathrm{p}[\mathrm{MA}]/(\pi a[\mathrm{m}]^2)$ is an empirical limit to consider for operational stability. Experiments have been able to demonstrate core density operation far above the Greenwald limit in scenarios with benign ELM activity [69]. This indicates that the Greenwald density is not a strict limit of the core plasma, but rather a limit more closely associated with pedestal or SOL behaviour. In the parameter scans of section 4, line averaged core densities are allowed to exceed the Greenwald limit by up to 20%. ELM stability is analysed separately for individual candidate flat-top operating points.

2.5. *Plasma current and internal inductance*

A high plasma current is beneficial for fusion power performance, since it allows access to higher densities and kinetic pressures at constant Greenwald fraction and β_N. However, the forces on surrounding vessel structures during disruption events scale as I_p^2, ultimately setting an upper limit to the safe operation of the plasma current. Other risks with high plasma currents also include runaway electrons, with a generation rate scaling exponentially with I_p, and current driven global MHD instabilities. The agreed upper limit of $I_\mathrm{p} = 25$ MA is based on current (limited) understanding of the ability to manage the above-mentioned risks, which means that the limit is likely to change in more mature stages of the design. In the scans of section 4, a slightly more conservative limit of $I_\mathrm{p} = 23$ MA has been chosen. This is because $I_\mathrm{p} < 25$ MA is satisfied in almost the entire scan spaces, whereas $I_\mathrm{p} < 23$ MA reveals domains of high current in multi-dimensional presentations of the scan space (see e.g. figure 7(*c*)).

A broad current density profile, resulting in a low internal inductance, is beneficial for vertical stability. The current density profile can be directly controlled using auxiliary current drive systems, and indirectly via the bootstrap current, which is influenced e.g. by the pressure peaking. The individual scan points of section 4 have not been checked against a vertical stability limit, since the auxiliary current drive has been extrapolated from the template simulations using simplifying assumptions (see section 3.6), without regard for the degrees of freedom of the systems for current profile shaping. On the other hand, in the development of the candidate flat-top points of section 5, the auxiliary systems have been tuned to result in a broad current profile and low l_i. Using the simple limit $\kappa_\mathrm{max} = 3.4 - l_\mathrm{i}$ [46] (the normalised inductance l_i is defined according to equation (10) in [70]), the STEP elongation $\kappa_{95} = 2.8$ would imply $l_\mathrm{i} < 0.6$ for vertical controllability. As shown in table 5, the achieved normalised inductance never exceeds 0.53. Vertical stability has been further verified with the free boundary equilibrium solver Fiesta [24].

In principle, there is a lower limit of the internal inductance related to the shaping of the separatrix inner and outer legs. For a given divertor and coil-set design, there has to exist a configuration of the coil currents such that the resulting separatrix shape is well optimised for the requirements of exhaust and detachment access (the radially extended outer leg and the inner leg X-divertor, as discussed in section 2.7). A flat current density profile, or more specifically a sharp edge gradient of the current density, makes the shaping of the separatrix legs less flexible. As a guideline, the limit $l_\mathrm{i}(3) \gtrsim 0.25$ can be assumed, based on simulations with the free boundary solver Fiesta. However, this is not a rigid limit, as the possibility to find viable separatrix solutions is more dependent on local plasma parameters, rather than on global parameters, such as $l_\mathrm{i}(3)$.

2.6. *Energy and particle confinement*

Turbulent transport in STEP high beta plasmas is expected to be electromagnetic and not to be well described by current state-of-the-art reduced core plasma transport models (e.g. TGLF [71] and QuaLiKiz [72]). In this paper, the modelled STEP scenarios will be guided using empirical models of the core transport. Computationally intensive first principles-based calculations of turbulent transport in STEP scenarios developed in this paper are reported in [16] and [18]. We proceed by comparing design points to empirical scalings of the confinement time in order to quantify the viability of the energy confinement implied by the transport assumptions. As a proxy, the ITER energy confinement scaling $\tau_\mathrm{IPB98(y,2)}$ [8] has been selected for assessing the confinement assumptions in this paper. Despite being based on conventional tokamaks, the scaling is developed from a relatively large database of experiments (more than 1300 H-mode pulses from nine different tokamaks), meaning that its validity spans a broad plasma parameter space. The aspect ratio of the tokamaks in the database stretches between 2.5 (DIII-D) and 5.5 (PBX-M).

The confinement assumption can be quantified by the confinement factor, defined as $H_\mathrm{IPB98(y,2)} = \tau_\mathrm{E}/\tau_\mathrm{IPB98(y,2)}$. Since the confinement is uncertain and has potential for optimisation, we seek the minimum confinement assumption that satisfies the other constraints for a non-inductive burning plasma. The scans of section 4 check the viability of the confinement assumption with fixed values of the maximum confinement factors. Two limiting values are selected: one 'conservative' limit of 1.2, and one 'optimistic' limit of 1.4. It is presently unknown whether realistic values of the confinement factor in STEP relevant regimes lie between, above or below these two values, making the specific limits somewhat arbitrary at present stages of the modelling. However, the limits are sufficient to provide guidelines for target regimes within the operational spaces set by other constraints. As will be demonstrated in sections 4 and 5, the conservative limit of 1.2 is possible to satisfy, but only with the high current drive efficiency of EBW, whereas the optimistic limit of 1.4 can also be satisfied in scenarios without EBW.

The ITER scaling of the confinement time $\tau_{\mathrm{IPB98(y,2)}}$ scales with respect to net power as $P_{\mathrm{net}}^{-0.69}$, where $P_{\mathrm{net}} = P_{\mathrm{tot}} - \mathrm{d}W_{\mathrm{th}}/\mathrm{d}t$, $P_{\mathrm{tot}} = P_{\mathrm{aux}} + P_{\alpha} + P_{\mathrm{ohm}}$ and W_{th} is the (thermal) stored energy. The scaling typically does not include contribution to P_{net} from the radiated power, under the assumption that $P_{\mathrm{rad}} \ll P_{\mathrm{tot}}$. However, this assumption does not hold for STEP plasmas, since a significant fraction of seeded impurity radiation is likely to be required for detachment access ($P_{\mathrm{rad}}/P_{\mathrm{tot}} \sim 0.7$). A radiation corrected confinement factor, here referred to as H_{98}^{*}, has been derived for highly core radiated plasmas using ASTRA/TGLF [15]. The definition replaces P_{net} with $P_{\mathrm{net}}^{*} = P_{\mathrm{net}} - \gamma P_{\mathrm{rad}}$ for some coefficient $0 < \gamma < 1$, meaning that $H_{98}^{*} = \tau_{\mathrm{E}}^{*}/\tau_{98}^{*} \propto (W_{\mathrm{th}}/P_{\mathrm{net}}^{*})/(P_{\mathrm{net}}^{*})^{-0.69} \propto (P_{\mathrm{net}} - \gamma P_{\mathrm{rad}})^{-0.31}$. A high γP_{rad} implies a high H_{98}^{*}, and vice versa. That is, if γP_{rad} is large, then high confinement is required in order to be consistent with a given density and temperature regime. The studies in [15] found that radiation in the deep core influences the confinement more than radiation closer to the separatrix. More specifically, γ can be estimated by taking 60% of the radiation inside $\rho_{\mathrm{tor}} = 0.75$ into account. Note that this γ was derived for the DEMO conventional tokamak, and it is presently unknown how well it extrapolates to STEP. For lack of better alternatives, it is used in the presented confinement assessments. Since the radiated power distribution is not self-consistently modelled during the parameter scans of section 4, $\gamma = 0.6$ is chosen, which is a conservative assumption in that it assumes all radiation to impact the confinement, and H_{98}^{*} is maximised. On the other hand, the derived flat-top points of section 5, which includes more self-consistent modelling of impurities and the radiated power distribution, only consider the radiation inside $\rho_{\mathrm{tor}} = 0.75$ in the P_{net}^{*} estimate.

Several empirical scaling laws suggest a weaker density scaling compared to $\tau_{\mathrm{IPB98(y,2)}} \propto \langle n_{\mathrm{e}} \rangle^{0.41}$, such as $\tau_{\mathrm{Petty08}} \propto \langle n_{\mathrm{e}} \rangle^{0.32}$ [73], $\tau_{\mathrm{ITPA20}} \propto \langle n_{\mathrm{e}} \rangle^{0.24}$ [74], and $\tau_{\mathrm{ITPA20-IL}} \propto \langle n_{\mathrm{e}} \rangle^{0.15}$ [74]. Scaling laws derived from ST databases even suggest a weakly negative scaling with respect to density, such as $\tau_{\mathrm{NSTX19}} \propto \langle n_{\mathrm{e}} \rangle^{-0.05}$ [10], and $\tau_{\mathrm{MAST09}} \propto \langle n_{\mathrm{e}} \rangle^{-0.06}$ [75]. However, most scaling laws are based on a smaller database of pulses than $\tau_{\mathrm{IPB98(y,2)}}$, in particular the purely ST based scaling laws. Nevertheless, given the uncertainty in the density scaling of confinement in STEP relevant regimes, it is prudent to explore the optimisation of operating points using several different scalings, and to design a machine that can accommodate a range of operating points at different densities.

Due to the opacity of the scrape-off layer to neutral gas, STEP will be dominantly pellet fuelled, unlike most present experiments. Empirical expectations of particle confinement are less readily available, and particle confinement time depends greatly on the location and type of the particle source. Because of the difficulty in quantifying neutral gas sources inside the separatrix, particle confinement time is rarely measured in tokamak experiments. However some perturbative experiments have been conducted with pellets [76, 77], and trace tritium NBI (into D) [78, 79], which measure the confinement time of a core fuelling source transient based on the subsequent decay time of density or neutron rate. The JET experiments with trace tritium NBI and gas perturbations found particle confinement times between 200 and 800 ms (3–4 times longer than the energy confinement time), with an inverse dependence on β. These experiments also experimentally inferred ion particle diffusivity lower than thermal conductivity and inward pinch velocity (as is routinely found in first principle turbulent transport models [80]). The MAST experiments [76] attempt to quantify a 'pellet retention time' by a similar methodology, which approaches or exceeds the energy confinement time in ELM-free plasmas (which STEP will be). This analysis is complicated by the large perturbation in the overall density profile and transport properties of a pellet in MAST. The individual pellet perturbations should be relatively smaller in STEP, and the dynamic effects of these perturbations on transport and particle confinement should be analysed in future work with a first principle transport model.

Based on these observations and models, we have assumed that STEP will have a pellet particle confinement time 3–4 times larger than the energy confinement time. If the particle transport assumptions used to design the present STEP scenarios later need updating, it will mostly result in a change in the pellet fuelling demand. Within a factor of two in either direction should not present a significant problem. If the particle confinement times prove to be an order of magnitude different from the present assumptions, it could present problems in either direction. Too low, and the tritium burn-up fraction will be too low, causing problems for the fuel cycle to reprocess and reinject enough tritium in burning steady-state. Too high, and helium ash is likely to accumulate, overwhelming the pumping capability and choking the fusion burn.

In the broader STEP modelling workflow, the operational points presented in section 5 were designed first, assuming confinement, and aiming to minimise the H_{98}^{*} required for a steady state scenario whilst satisfying the other constraints for the flat-top operating point. These scenarios were then analysed with gyrokinetics, leading to flux driven predictions of confinement [19] that are close to the EC-HD case in section 5. Future iterations of the scenarios will update the transport assumptions based on the gyrokinetic results, and optimise the magnetic equilibrium and q-profile to improve the confinement; this process will require iteration between the integrated modelling presented here and the gyrokinetic workflow of [19].

2.7. Power losses and detachment access

STEP will need to operate with a detached plasma in most phases of operation to provide sufficient protection of the divertor. The peak heat loads associated with an attached divertor plasma would far exceed the expected engineering limits of $\sim 10\,\mathrm{MW\,m^{-2}}$ in steady-state. The operational challenge is to integrate the detachment with the plasma core, and to make the detached plasma operation robust to small fluctuations of the plasma. Some of the present exhaust assumptions and limitations have been further addressed using SOL, wall and divertor modelling with SOLPS-ITER [25]. Since JETTO is a core plasma model, boundary conditions in e.g. temperature, density and impurity fraction need to be applied at the last closed flux surface, with no indication of whether the applied conditions are compatible with a divertor plasma solution. However, a reduced model of the SOL and divertor can be coupled to JETTO to provide more realistic boundary constraints, while also assessing the detachment requirements at the divertor. This can provide a useful check for operational regimes in the JETTO parameter scans of section 4, since it is unfeasible to complement every single scan point with detailed exhaust analyses from more advanced, computationally heavy SOL/divertor models.

Detachment access can be estimated using a detachment qualifier [81]

$$q_{\mathrm{det}} = 1.3\frac{P_{\mathrm{sep}}\,[\mathrm{MW}]}{R_{\mathrm{geo}}\,[\mathrm{m}]}\frac{5\,\mathrm{mm}}{\lambda_{\mathrm{int}}\,[\mathrm{mm}]}\left(\frac{1.65\,\mathrm{m}}{R_{\mathrm{geo}}\,[\mathrm{m}]}\right)^{0.1} \times\left(\left[1+\sum_Z f_Z c_{Z,\mathrm{div}}\right]p_{0,\mathrm{div}}\,[\mathrm{Pa}]\right)^{-1}, \qquad (5)$$

where detachment is accessed at $q_{\mathrm{det}} < 1$ and partial detachment at $q_{\mathrm{det}} \approx 1$. λ_{int} is the SOL power width with the effect of power spreading taken into account ($\lambda_{\mathrm{int}} = \lambda_q + 1.64 S_{\mathrm{PS}}$, S_{PS} is the power spreading factor [82]). f_Z is the radiation efficiency of impurity Z relative to deuterium, and $c_{Z,\mathrm{div}}$ is the concentration of the impurity in the divertor region. $p_{0,\mathrm{div}}$ is the divertor neutral pressure. It should be pointed out that the specific expression of equation (5) was derived for ASDEX Upgrade, with the overall factor 1.3 depending on the specifics of the divertor configuration (conventional single null geometry). The double null geometry and the radially extended outer strike-point of STEP reduce this factor. Deriving an exact correction to the factor is out of scope for this paper. Rather, the 1.3 overall factor can be used as a conservative value (a larger overall factor reduces the operational space that satisfies $q_{\mathrm{det}} < 1$).

Argon is planned to be the primary impurity species seeded for detachment control in STEP, which is expected to have a radiation efficiency $f_{\mathrm{Ar}} = 90$ [81]. STEP needs to operate with the minimal amount of argon that is still sufficient to reach the required degree of detachment, since even a small amount of argon leaking into the core can substantially degrade the fusion power performance by dilution ($P_{\mathrm{fus}} \propto (1-18c_{\mathrm{Ar,core}})^2$, e.g. 0.5% of argon reduces the fusion power by more than 17%). Reduced core ion temperature resulting from impurity radiation also risks reducing the fusion reaction cross section. The level of screening of argon from the core can be quantified with the enrichment factor $\eta_Z = (n_{Z,0,\mathrm{div}}/n_{\mathrm{D},0,\mathrm{div}})/(n_{Z,\mathrm{core}}/n_{\mathrm{e,core}})$ (subscript 0 refers to neutral density). Experiments at ASDEX Upgrade have demonstrated an argon enrichment factor $\eta_Z \approx 2$ [83]. A higher enrichment factor is expected for STEP due to neoclassical screening in the pedestal [84, 85]. A current estimate of the maximum $c_{\mathrm{Ar,div}}$ without unacceptable dilution in the core is 2%–3%.

Other parameters that play a role in the detachment access according to equation (5) are $P_{\mathrm{sep}}/R_{\mathrm{geo}}$, λ_{int} and $p_{0,\mathrm{div}}$. An upper limit of $P_{\mathrm{sep}}/R_{\mathrm{geo}} = 45\,\mathrm{MW\,m^{-1}}$ (corresponding to $P_{\mathrm{sep}} = 45\times 3.6 = 162\,\mathrm{MW}$) has been chosen to define the operational domain in the scans of section 4. In order for the limit to correspond to $q_{\mathrm{det}} = 1$ in equation (5), it is assumed that $(1+90c_{\mathrm{Ar,div}})\lambda_{\mathrm{int}}p_{0,\mathrm{div}} \approx 270\,\mathrm{mmPa}$. An example of a combination of assumptions compatible with this number is $c_{\mathrm{Ar,div}} = 2.9\%$, $\lambda_{\mathrm{int}} = 5.0\,\mathrm{mm}$, and $p_{0,\mathrm{div}} = 15\,\mathrm{Pa}$. These are all values believed to be compatible with core and edge operational constraints under current assumptions. However, λ_{int}, and $p_{0,\mathrm{div}}$ are challenging to estimate in the present stages of modelling, requiring more self-consistent pump, SOL, impurity seeding and transport, and overall core confinement modelling to narrow down uncertainties. Later iterations of the divertor design are also likely to shift these parameter values. Despite inherent inaccuracies of the correspondence between the $P_{\mathrm{sep}}/R_{\mathrm{geo}} < 45\,\mathrm{MW\,m^{-1}}$ limit and the domain of detachment access, it remains a useful guideline, since P_{sep} is straightforward to evaluate in the present stages of core plasma modelling.

2.8. Summary of parameters and their constraints

The operational limits that are considered for all of the scans are the following:

(i) $1.5\,\mathrm{GW} \leqslant P_{\mathrm{fus}} \leqslant 1.8\,\mathrm{GW}$,
(ii) $Q_{\mathrm{sci}} \geqslant 11$,
(iii) $I_{\mathrm{p}} \leqslant 23\,\mathrm{MA}$,
(iv) $C_\beta \leqslant 0.5$,
(v) $P_{\mathrm{sep}}/R_{\mathrm{geo}} \leqslant 45\,\mathrm{MW\,m^{-1}}$,
(vi) $H^*_{98} \leqslant 1.2$ (conservative) or $H^*_{98} \leqslant 1.4$ (optimistic).

In addition, access to EC 2nd harmonic O-mode and EBW fundamental lower X-mode coupling is considered, according to the cut-off domains estimated in section 2.3. Additional constraints follow from the above assumptions, e.g.

$P_{\mathrm{aux}} \leqslant 163.6\,\mathrm{MW}$ ($P_{\mathrm{fus}} \leqslant 1.8\,\mathrm{GW}$ and $Q_{\mathrm{sci}} \geqslant 11$), and $P_{\mathrm{sep}} \leqslant 162\,\mathrm{MW}$ ($P_{\mathrm{sep}}/R_{\mathrm{geo}} \leqslant 45\,\mathrm{MW\,m^{-1}}$ and $R_{\mathrm{geo}} = 3.6\,\mathrm{m}$).

For the individual operating points presented in section 4, some other constraints are checked as well. Among these are:

(i) $q_{\mathrm{min}} \geqslant 2.2$,
(ii) $l_{\mathrm{i}} \leqslant 0.6$,
(iii) $f_{\mathrm{GW}} \leqslant 100\%$.

In addition, there are some less quantifiable constraints, e.g. MHD stability (analysed with MISHKA and MARS-F MHD codes), consistency of the pedestal solution with ideal ballooning theory (analysed with Europed), and a separatrix solution consistent with the suggested coil-set and divertor geometry (analysed with Fiesta). A more accurate analysis of vertical stability than the simple criterion $l_{\mathrm{i}} \leqslant 0.6$ has also been carried out with Fiesta. As mentioned in section 2.4, the empirical $f_{\mathrm{GW}} \leqslant 100\%$ limit can in principle be exceeded. However, the presented candidate flat-top points have all been chosen to satisfy this limit.

Parameters that are held fixed throughout the presented modelling, effectively being operational constraints, are

(i) $V_{\mathrm{loop}} = 0$ (fully non-inductive operation),
(ii) geometry of the last closed flux surface,
    - implies parameters such as R_{geo}, a_{min}, κ (elongation), and δ (triangularity),
(iii) vacuum toroidal magnetic field at R_{geo}: B_{geo},
(iv) separatrix boundary conditions in
    - deuterium and tritium densities,
    - electron and ion temperatures.

3. Integrated core plasma modelling with JETTO

To examine steady-state flat-top scenarios, we use JETTO in assumption integration mode, in which confinement is assumed. In this way of running JETTO, anomalous heat and particle transport is not predicted from turbulent physics. Rather, a target regime in density and temperature is set, and the anomalous transport is artificially rescaled until the target is reached. Section 3.3 presents this approach and its motivation in more detail. The main model inputs are:

- size and shape of the separatrix
- densities and temperatures at the separatrix
- vacuum toroidal magnetic field at $R = R_{\mathrm{geo}}$: B_{geo}
- normalised beta: $\beta_{\mathrm{N}} = \beta_{\mathrm{N,th}} + \beta_{\mathrm{N,fast}}$
- relative electron to ion anomalous heat diffusivity
- Greenwald density fraction, $f_{\mathrm{GW}} = \langle n_{\mathrm{e}} \rangle / n_{\mathrm{GW}}$
- auxiliary power densities: q_{EC} and q_{EBW} $[\mathrm{W\,m^{-3}}]$
- EC current drive efficiency: ζ_{CD},
- EBW current density: J_{EBW}.

Some of the main outputs are:

- plasma current density: J_{p} $[\mathrm{A\,m^{-2}}]$
    - predicted from bootstrap current J_{BS}, EC current drive J_{EC} and (prescribed) EBW current J_{EBW}
- heat and particle transport
    - neoclassical is predicted, and anomalous is artificially rescaled
- kinetic profiles (densities & temperatures)
- fusion power density: q_{fus}
- alpha heating: $q_{\alpha,\mathrm{e}}$ and $q_{\alpha,\mathrm{i}}$
- 2D magnetic equilibrium: $B_R(R,z)$, $B_z(R,z)$ and $B_{\mathrm{tor}}(R,z)$
- power flux across the separatrix: P_{sep}.

There are some differences between the modelling assumptions of the parameter scans of section 4 and the list of candidate flat-top operating points in section 5, which impacts some of the set of inputs and outputs. For instance, the radiation fraction $f_{\mathrm{rad}} = P_{\mathrm{rad}}/(P_{\mathrm{aux}} + P_\alpha + P_{\mathrm{ohm}})$ and the effective charge $Z_{\mathrm{eff}} = \sum_i Z_i^2 n_i / \sum_i Z_i n_i$ are inputs in the scans, but they are outputs in the candidate flat-top calculation. Details on this is outlined in section 3.7.

3.1. Scan templates

The parameter scans of section 4 are done by varying key plasma parameters relative to a given reference case, here referred to as a scan template. Two different scan templates are used, which are based on the two different auxiliary heating and current drive schemes that are suggested for STEP. Consequently, these are referred to as the EC template [86] and the EC+EBW template [87]. A summary of 0D data for the two templates is presented in table 2. The auxiliary heating power and current drive profiles for the two scan templates, together with electron densities and temperatures, are shown in figure 3.

All of the simulations presented in this paper target single stationary flat-top operating points, rather than dynamical scenarios. Each simulation is continued until outputs have sufficiently converged in time. Since current diffusion time scales are of the order 10^3 s in most of the plasma, the plasma resistivity in the current diffusion equation has been artificially scaled up by a constant factor. This scaling should not impact the outcome of converged solution. A set of example outputs from a JETTO simulation is presented in figure 4(the particular simulation presented in the figure is the EC template).

3.2. Equilibrium and boundary conditions

A fixed separatrix geometry is assumed in JETTO (see figure 5), which has been calculated by the free boundary equilibrium solver Fiesta [37] from a given coil-set geometry. Since JETTO is a core plasma model, particle and power fluxes cannot be evaluated beyond the separatrix. SOLPS-ITER [45]

Table 2. Summary of 0D outputs from the two template simulations.

		EC [86]	EC+EBW [87]
P_{fus}	[GW]	1.65	1.77
Q_{sci}	[ ]	10.94	13.60
P_{EC}	[MW]	150.00	9.00
P_{EBW}	[MW]	—	120.00
$\langle n_{\mathrm{e}} \rangle$	$[10^{19}\ \mathrm{m}^{-3}]$	15.40	17.35
$\langle n_{\mathrm{e}} \rangle_{\mathrm{line}}/n_{\mathrm{GW}}$	[%]	100.13	100.02
$\langle T_{\mathrm{e}} \rangle$	[keV]	9.81	9.05
$\langle T_{\mathrm{i}} \rangle / \langle T_{\mathrm{e}} \rangle$	[ ]	1.07	1.04
I_{p}	[MA]	20.10	22.88
$I_{\mathrm{BS}}/I_{\mathrm{p}}$	[%]	87.88	81.74
I_{EC}	[MA]	2.17	0.15
I_{EBW}	[MA]	—	3.95
$I_{\mathrm{EC}}/P_{\mathrm{EC}}$	$[\mathrm{kA\,MW}^{-1}]$	14.48	16.14
$I_{\mathrm{EBW}}/P_{\mathrm{EBW}}$	$[\mathrm{kA\,MW}^{-1}]$	—	32.89
β_{N}	[ ]	4.40	3.93
B_{axis}	[T]	2.59	2.57
l_{i}	[ ]	0.50	0.39
$l_{\mathrm{i}}(3)$	[ ]	0.28	0.22
q_{min}	[ ]	2.18	3.14
q_{95}	[ ]	9.35	8.00
P_{rad}	[MW]	336.02	336.72

is used to predict the SOL plasma and fluxes on plasma facing components and the divertors. Densities and temperatures are given as fixed boundary conditions at the separatrix, with the values $T_{\mathrm{e,sep}} = 160\,\mathrm{eV}$, $T_{\mathrm{i,sep}} = 400\,\mathrm{eV}$, $n_{\mathrm{D,sep}} = 1.5 \times 10^{19}\,\mathrm{m}^{-3}$, $n_{\mathrm{T,sep}} = 1.5 \times 10^{19}\,\mathrm{m}^{-3}$. These values have been suggested from iterations between JETTO and SOLPS-ITER. It should be noted that the relatively high $T_{\mathrm{i,sep}}/T_{\mathrm{e,sep}} = 2.5$ is mainly valid in scenarios with low D_2 and T_2 gas puffing and high edge impurity seeding rates, which is not an applicable assumption to all scenarios presented in this paper. However, with the way that the pedestal modelling is set-up (see section 3.5), the converged plasma solution has very limited sensitivity to the assumed temperature boundary conditions. In later stages of the STEP modelling, JETTO and EDGE2D/EIRENE [88, 89] will be integrated at runtime via the JINTRAC [90] integrated modelling framework, which will give more self-consistent estimates of the separatrix densities and temperatures via direct interaction between the core and the SOL plasmas. There are differences in how the impurity densities and their boundary conditions are handled between the scans and the candidate flat-top points, which is discussed in section 3.7. Electron density simply follows from quasi-neutrality assumption. The magnetic equilibrium inside the separatrix is calculated self-consistently in JETTO using the ESCO [31] 2D Grad-Shafranov solver.

3.3. Transport and confinement

The expected transport and overall confinement of the plasma in STEP relevant regimes are presently unknown. Available empirical scalings lack validity in these regimes, and extrapolation of them arrives at different conclusions regarding the confinement and its dependencies with respect to key plasma parameters. Gyrokinetic modelling has shed some light on the kinds of turbulence that are expected to dominate [13, 16, 18, 19, 91], but more extensive nonlinear modelling is required to predict the overall confinement accurately. The micro-scale turbulence is expected to be electromagnetic, dominated by kinetic ballooning and micro-tearing modes. With JETTO run in assumption integration mode, the density and temperature regimes are essentially defined as inputs to the code, and fuelling rates and anomalous transport are rescaled in feedback loops until the target regimes have been reached. This way, a broad range of plasma regimes can be assessed in terms of fusion power performance and engineering limitations. The confinement assumption can then be further analysed using some of the available empirical scaling laws. The fuelling rate is adapted to reach a target Greenwald density fraction $f_{\mathrm{GW}} = \langle n_{\mathrm{e}} \rangle / n_{\mathrm{GW}}$ (more details in section 3.4), whereas the anomalous heat and particle diffusivities are rescaled to reach a target normalised beta β_{N}.

Heat and particle transport both have a neoclassical component computed by NCLASS [92], which has not been rescaled. To get a sensible shape of the anomalous heat diffusivity profiles, the Bohm/gyro-Bohm [93] semi-empirical transport model has been used. The relative electron to ion heat diffusivities are tuned to have dominant electron heat transport, motivated by recent ST experiments [20] and gyrokinetic simulations of relevant regimes [16–19]. Since ions and electrons are well coupled in STEP regimes, the design points are not very sensitive to the ratio of ion to electron heat transport assumed. The anomalous heat diffusivities are evaluated according to

$$\chi_{\mathrm{e,anom}} = \alpha_{\mathrm{BgB}} \left(0.01 \chi_{\mathrm{e,B}} + 50 \chi_{\mathrm{e,gB}} \right), \tag{6}$$

$$\chi_{\mathrm{i,anom}} = \alpha_{\mathrm{BgB}} \left(0.001 \chi_{\mathrm{i,B}} + \chi_{\mathrm{i,gB}} \right), \tag{7}$$

where α_{BgB} is the transport rescaling parameter, adapted to reach a given target β_{N}. The JETTO implementation of the individual Bohm/gyro-Bohm coefficients are

$$\chi_{\mathrm{e,B}} = \chi_{\mathrm{i,B}}/2 = \alpha_{\mathrm{B}} \frac{a_{\mathrm{min}} q^2}{e B_{\mathrm{ax}} n_{\mathrm{e}}} \sqrt{\frac{\pi B_{\mathrm{geo}}}{\Psi_{\mathrm{tor,sep}}}} \left| \frac{\partial p_{\mathrm{e}}}{\partial \rho_{\mathrm{tor}}} \right|, \tag{8}$$

$$\chi_{\mathrm{e,gB}} = 2 \chi_{\mathrm{i,gB}} = \alpha_{\mathrm{gB}} \frac{\sqrt{T_{\mathrm{e}}}}{B_{\mathrm{ax}}^2} \sqrt{\frac{\pi B_{\mathrm{geo}}}{\Psi_{\mathrm{tor,sep}}}} \left| \frac{\partial T_{\mathrm{e}}}{\partial \rho_{\mathrm{tor}}} \right|, \tag{9}$$

where $\alpha_{\mathrm{B}} = 2 \times 10^{-4}$ and $\alpha_{\mathrm{gB}} = 5 \times 10^{-6}\,\mathrm{T}^2\mathrm{m}^3/\mathrm{eV}^{3/2}\mathrm{s}$ are empirical constants, and $\Psi_{\mathrm{tor,sep}}$ is the toroidal magnetic flux at the separatrix, offset such that $\Psi_{\mathrm{tor,ax}} = 0$. The particular choice of the scaling coefficients in equations (6) and (7) effectively results in neoclassical diffusivities similar to or larger than the anomalous diffusivity. As pointed out in section 2.6, further iterations between the integrated core plasma modelling presented here and the gyrokinetic workflow of [19] will be required to gradually refine the anomalous transport assumtions.

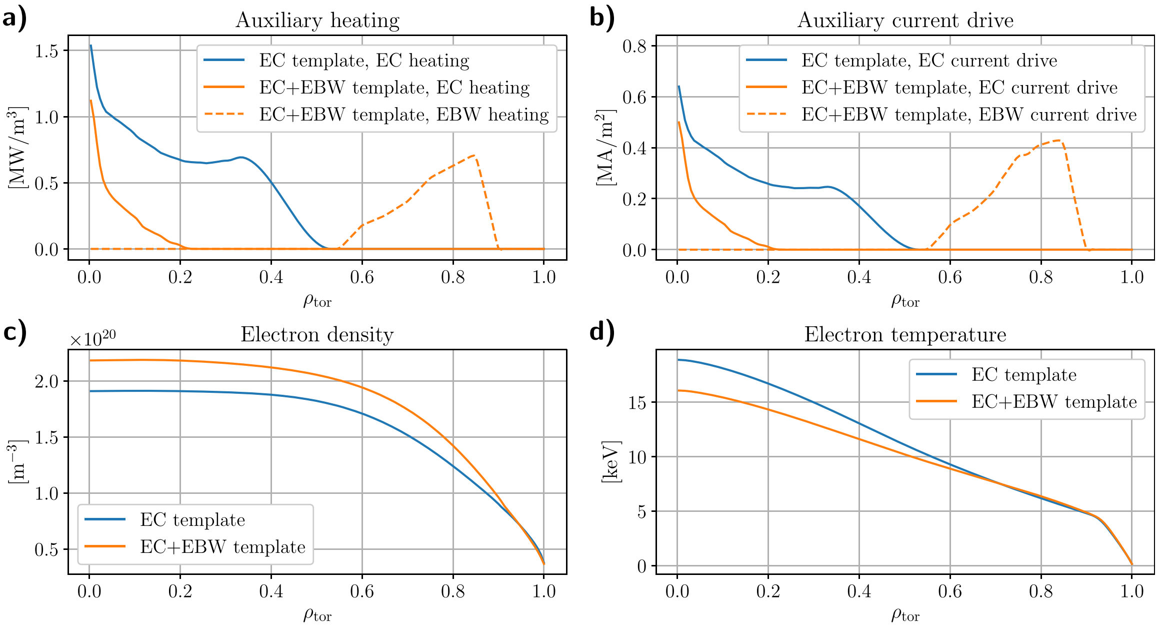

Figure 3. Top figures: auxiliary heating and current drive for the two template simulations used in the scans. Bottom figures: electron density and temperature for the template simulations.

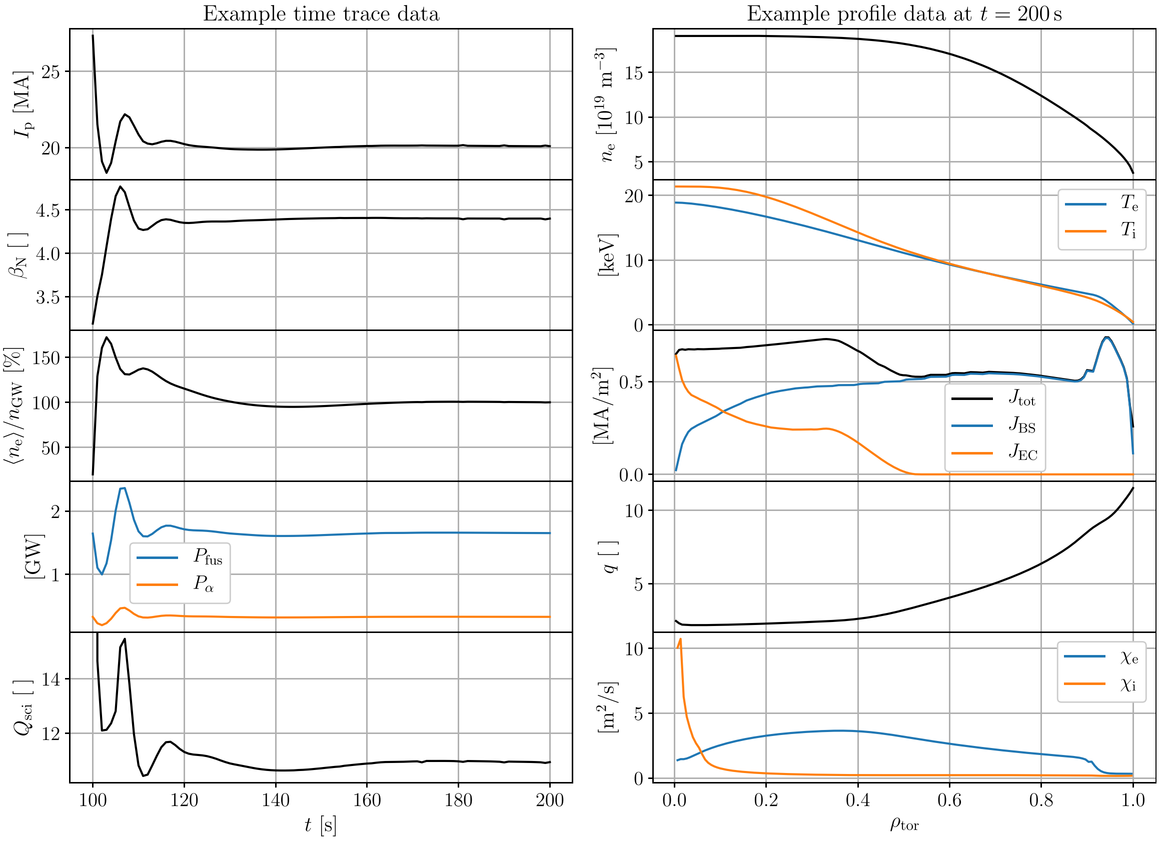

Figure 4. Selection of JETTO outputs from the EC template simulation. $\rho_{\rm tor}$ is the square root of the normalised toroidal magnetic flux.

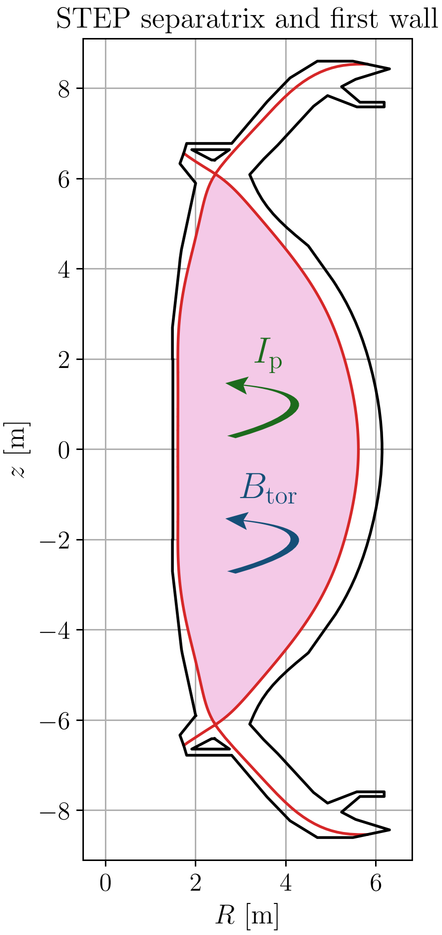

Figure 5. Separatrix geometry assumed for the JETTO simulations, generated with the free equilibrium solver Fiesta [37]. Arrows show the orientation of the toroidal magnetic field and the plasma current (both are counterclockwise when viewed from above).

Anomalous particle diffusivities are derived from anomalous heat diffusivities according to

$$D_\mathrm{p,anom} = \xi\left(\rho_\mathrm{tor}\right)\frac{\chi_\mathrm{e,anom}\chi_\mathrm{i,anom}}{\chi_\mathrm{e,anom}+\chi_\mathrm{i,anom}}, \tag{10}$$

$$\xi\left(\rho_\mathrm{tor}\right) = A_1 + \left(A_2 - A_1\right)\rho_\mathrm{tor}, \tag{11}$$

where $A_1 = 1.0$ and $A_2 = 0.3$. The linear weight function $\xi(\rho_\mathrm{tor})$ and its parameter values A_1 and A_2 correspond to an ad hoc rescaling of the particle diffusivity that agrees with transport modelling of JET experiments. Because of the low ion heat diffusivity, which is close to neoclassical levels, the resulting particle diffusivity is also almost purely neoclassical at higher β_N values. There is an additional inward particle pinch term,

$$v_\mathrm{in} = 0.5\frac{D_\mathrm{p}S_\mathrm{flux}^2}{V}\left(\frac{\mathrm{d}V}{\mathrm{d}\rho_\mathrm{tor}}\right)^{-1}\sqrt{\frac{\Psi_\mathrm{tor,sep}}{\pi B_\mathrm{geo}}}, \tag{12}$$

which has also been observed to agree with Bohm/gyro-Bohm modelling of JET experiments. Here, S_flux is the flux surface area, $V(\rho_\mathrm{tor})$ is the volume contained inside ρ_tor. The resulting particle confinement times are later checked against the assumptions in section 2.6.

3.4. Fuelling

The target Greenwald density fraction is reached by feedback on the particle source rate, mimicking pellet fuelling with a simple source density that is Gaussian in $\rho_\mathrm{tor} = \sqrt{\Psi_\mathrm{tor}/\Psi_\mathrm{tor,sep}}$ and continuous in time. The Gaussian is centred at $\rho_\mathrm{tor} = 0.8$, with a width $\sigma_\rho = 0.24/\sqrt{2} \approx 0.17$. The depth and width of the pellet deposition has been guided by calculations with HPI2 [94] discrete pellet model using realistic pellet injector location and geometry.

3.5. Pedestal and edge transport barrier

Based on Europed [41] modelling of STEP relevant scenarios, the electron pressure pedestal height is scaled according to

$$p_\mathrm{e,ped}\,[\mathrm{Pa}] = c_p\left(n_\mathrm{e,ped}\left[10^{19}\,\mathrm{m}^{-3}\right]\right)^{0.4}\left(I_\mathrm{p}\,[\mathrm{MA}]\right)^{1.44} \\ \times\left(B_\mathrm{geo}\,[\mathrm{T}]\right)^{0.41}\left(R_\mathrm{geo}\,[\mathrm{m}]\right)^{-2.1}\left(\delta\,[\,]\right)^{1.69}, \tag{13}$$

where $c_p = 2.728 \times 10^3$, and δ is the triangularity of the last closed flux surface. The ion pressure is assumed to follow the same scaling. A correction factor of 0.9 is applied to $p_\mathrm{e,ped}$ to ensure a regime with small or no ELMs (see details in [11]). The pedestal width in normalised poloidal flux follows the scaling

$$\Delta_\mathrm{ped} = 0.1\beta_\mathrm{pol,ped}^{1/2}, \tag{14}$$

where $\beta_\mathrm{pol,ped} = 4\mu_0 p_\mathrm{e,ped}/\langle B_\mathrm{pol}\rangle^2$ is the poloidal beta, evaluated at the pedestal. The width scaling of equation (14) is the same as in [95], but with a prefactor 0.1 instead of 0.076. The pedestal height is set by adjusting the anomalous thermal diffusivities in the edge transport barrier domain, $\psi_\mathrm{pol}/\psi_\mathrm{pol,sep} < 1 - \Delta_\mathrm{ped}$, on feedback until the target pressure at the pedestal top (equation (14)) is reached. A corresponding transport barrier in the anomalous particle diffusivity follows via the relationship in equation (10). A smoothening of the diffusivities across the edge transport barrier is applied, as shown in the example in figure 6. The characteristic width of the smoothening Δ_smooth is set to the width in ρ_tor that corresponds to 4 cm in the outer mid-plane.

All presented simulations, including individual parameter scan points and candidate flat-top operating points, have assumed H-mode confinement. To verify this assumption, P_sep has been compared against the ITPA empirical L–H power threshold [96], corrected for DT-plasmas [97]:

$$P_\mathrm{L-H}\,[\mathrm{MW}] = 0.0488\left(\langle n_\mathrm{e}\rangle_\mathrm{line}\left[10^{20}\,\mathrm{m}^{-3}\right]\right)^{0.717}\left(B_\mathrm{ax}\,[T]\right)^{0.803} \\ \times\left(S_\mathrm{LCFS}\left[\mathrm{m}^2\right]\right)^{0.941}\frac{2\left(\langle n_\mathrm{D}\rangle + \langle n_\mathrm{T}\rangle\right)}{2\langle n_\mathrm{D}\rangle + 3\langle n_\mathrm{T}\rangle}, \tag{15}$$

where S_LCFS is the area of the last closed flux surface.

3.6. Heating and current drive

Since the steady-state current is provided entirely by auxiliary heating systems and the bootstrap current, the total plasma

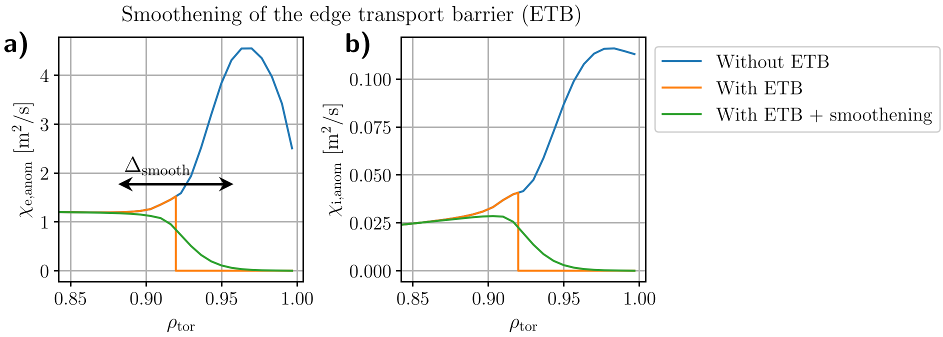

Figure 6. Example of edge transport barrier smoothening. (*a*) Anomalous electron diffusivity. (*b*) Anomalous ion diffusivity.

current is an output of the simulations. The bootstrap component is predicted with NCLASS [92] neoclassical model. Alpha heating, including split of heating fraction between electrons and ions, is based on an analytic model described in [98], and the model for slowing-down distribution with the resulting alpha particle pressure is described in [99].

At the template simulations for the parameter scans, the EC and EBW heating and current density profiles have been chosen to agree with results from beam-tracing codes GRAY [38] and GENRAY [39], and kinetic Fokker–Planck solver CQL3D [40]. None of these codes are used at runtime during the scans; GENRAY and CQL3D have not been integrated with JETTO, and GRAY is too computationally demanding to use for all (more than 1400) scan points. Instead, the codes have been used in a narrow parameter space around the template points to understand the trends of heating and current drive with respect to plasma parameters, which have then been translated to simplified assumptions that are used by JETTO in the scans. The spatial dependence of the heating power density is kept fixed in the scans, with an overall scaling factor proportional to the power of the auxiliary system. The dependencies of the current drive with respect to auxiliary power and plasma parameters are handled differently for the EC and EBW systems.

The flux surface averaged toroidal EC current density in JETTO is evaluated according to

$$J_{\mathrm{EC}}\left[\mathrm{A/m^2}\right] = \zeta_{\mathrm{CD}} P_{\mathrm{EC}}\,[\mathrm{MW}]\,\Sigma\left[\mathrm{m^{-2}}\right]\frac{T_{\mathrm{e}}\,[\mathrm{eV}]}{n_{\mathrm{e}}\left[10^{19}\,\mathrm{m^{-3}}\right]}, \tag{16}$$

where ζ_{CD} is a global parameter quantifying the current drive efficiency, and Σ is a factor defined from the EC power density p_{EC} and the cross-sectional flux surface area S as

$$\Sigma\left(\rho_{\mathrm{tor}}\right) = \frac{\rho_{\mathrm{tor}} p_{\mathrm{EC}}}{\mathrm{d}S/\mathrm{d}\rho_{\mathrm{tor}}}\left(\int_0^1 \mathrm{d}\rho_{\mathrm{tor}}\,\rho_{\mathrm{tor}} p_{\mathrm{EC}}\left(\rho_{\mathrm{tor}}\right)\right)^{-1}. \tag{17}$$

The variation in current drive efficiency due to changes in the velocity space interaction of collisions is captured in the $T_{\mathrm{e}}/n_{\mathrm{e}}$ dependence of equation (16). By using equations (16) and (17), the current density profile J_{EC} is calculated from p_{EC}, n_{e}, T_{e} and ζ_{CD} (see example in figure 3, solid curves). For the EC template, ζ_{CD} is set to 18.2[4], whereas the EC+EBW template uses $\zeta_{\mathrm{CD}} = 22.7$ for the EC current drive. These values are in quantitative agreement with results from GRAY [38] current drive modelling. Comparing this to the more conventional definition of the current drive efficiency $\tilde{\zeta}_{\mathrm{CD}}$ used in the literature [100], it can be shown that

$$\tilde{\zeta}_{\mathrm{CD}} = \tilde{c}_0 R_{\mathrm{geo}}\,[\mathrm{m}] \times \left[\frac{n_{\mathrm{e}}}{T_{\mathrm{e}}}\left(\int_0^1 \mathrm{d}\rho_{\mathrm{tor}}\,\rho_{\mathrm{tor}} p_{\mathrm{EC}}\right)^{-1}\int_0^1 \mathrm{d}\rho_{\mathrm{tor}}\,\frac{\rho_{\mathrm{tor}} p_{\mathrm{EC}} T_{\mathrm{e}}}{n_{\mathrm{e}}}\right]\zeta_{\mathrm{CD}}, \tag{18}$$

where $\tilde{c}_0 \approx 3.27 \times 10^{-3}$. Note that $\tilde{\zeta}_{\mathrm{CD}}$ is a local quantity (a function of ρ_{tor}), taking values corresponding to a scalar times $n_{\mathrm{e}}/T_{\mathrm{e}}$. Its value has the most relevance in the parts of the plasma where the EC current is driven, which is also where the power density $p_{\mathrm{EC}}(\rho_{\mathrm{tor}})$ becomes large. Assuming for simplicity that the power density can be described by a single localised peak in ρ_{tor}, the expression within the square brackets of equation (18) becomes close to 1 in the volume of the peak (it becomes exactly 1 when p_{EC} is described by a single Dirac delta function in ρ_{tor}). A global current drive efficiency parameter, here referred to as $\tilde{\zeta}^{*}_{\mathrm{CD}}$, can then be defined with a close relationship to the JETTO parameter ζ_{CD} according to

$$\tilde{\zeta}^{*}_{\mathrm{CD}} = \tilde{c}_0 R_{\mathrm{geo}} \zeta_{\mathrm{CD}}. \tag{19}$$

This parameter takes the values 0.215 and 0.268 for the two templates, respectively.

Each parameter scan in section 4 assumes the same value of ζ_{CD} (and $\tilde{\zeta}^{*}_{\mathrm{CD}}$ by extension) as in the corresponding scan template. This assumption is valid given that the EC wave is absorbed in the same way for all scan points. A violation of this assumption would for instance be if the wave passes through a different set of harmonic resonances and cut-off layers before being absorbed at the target resonance. Scan points

---

[4] Note that ζ_{CD} has the unit $10^{13}\,\mathrm{A\,eV^{-1}\,W^{-1}\,m^{-3}} \approx 6.242 \times 10^{31}\,\mathrm{s^5\,m^{-7}\,kg^{-2}\,A}$, and $\tilde{c}_0$ has the unit $10^{-13}\,\mathrm{A^{-1}\,eV\,W\,m^2} \approx 1.602 \times 10^{-32}\,\mathrm{s^{-5}\,m^6\,kg^2\,A^{-1}}$. When presenting numerical values of ζ_{CD} and $\tilde{c}_0$, these units have been omitted for simplicity.

where the on-axis density exceeds the relevant cut-off density are flagged as being outside operational regimes (see details in section 2.3).

The EBW current drive density profile used in the EC+EBW template have been taken from results with GENRAY/CQL3D. Even though the EBW current drive density does not strictly follow equation (16), the area integrated version of the equation can be used in combination with equation (19) to derive an approximation of the normalised current drive efficiency for the EBW current drive to give an idea of how the efficiency compares to ECCD, which yields $\zeta_{\mathrm{CD}} \approx 72$, or $\tilde{\zeta}_{\mathrm{CD}} \approx 0.85$. However, ζ_{CD} cannot be assumed to be constant throughout the scan space, since the underlying physics is very different from EC heating and current drive. Studies of EBW current drive efficiency using GENRAY/CQL3D in a local density and temperature domain ($\sim$10% variation) around the EC+EBW template point at a fixed EBW power resulted in a nearly constant EBW current. The scans that were based on the EC+EBW template (sections 4.3 and 4.4) assume that $I_{\mathrm{EBW}}/P_{\mathrm{EBW}}$ is fixed at the template value of 32.89 kA MW^{-1}.

3.7. Impurities and radiation

The main impurities expected for STEP core plasmas are helium, xenon and argon. Helium results as ash from the D/T fusion reactions. Xenon is introduced via doped fuelling pellets to increase core radiation to the levels required for detachment access. Argon is likewise injected to assist detachment access, which is done by gas puffing in the divertor region (see details in section 2.7). The candidate flat-top points of section 5 model impurity densities and radiation self-consistently. Impurity transport is handled the same way as the main ions (see section 3.3), with the neoclassical transport expected to dominate. Atomic physics and the resulting impurity radiation is modelled by SANCO [101].

Simplifying assumptions are made for the impurity densities and radiation during the scans, since self-consistent treatment of the impurities is computationally demanding to a degree that is not viable for all 1400+ scan points. Impurity radiation is prescribed via the radiation fraction $f_{\mathrm{rad}} = P_{\mathrm{rad}}/(P_{\mathrm{aux}} + P_{\alpha} + P_{\mathrm{ohm}})$, which is set to 70% in all scan points unless stated otherwise. The radiation density is constant in space ($q_{\mathrm{rad}} = P_{\mathrm{rad}}/V$). Xenon and helium impurities are included in the core to account for dilution of the plasma. The impurity densities are set by a fixed $Z_{\mathrm{eff}} = 2.8$ and a fixed helium to xenon ratio $n_{\mathrm{He}}/n_{\mathrm{Xe}} = 152$. Furthermore, JETTO assumes full ionisation of both helium and xenon in this simplified description of impurities. The fixed Z_{eff} and $n_{\mathrm{He}}/n_{\mathrm{Xe}} = 152$ values are then equivalent to a helium concentration $n_{\mathrm{He}}/n_{\mathrm{e}} = (Z_{\mathrm{eff}} - 1) \times 76/1583 \approx 8.64\%$ and a xenon concentration $n_{\mathrm{Xe}}/n_{\mathrm{e}} = (Z_{\mathrm{eff}} - 1)/3166 \approx 5.69 \times 10^{-4}$, which matches the expected dilution from self-consistent impurity modelling in order of magnitude.

4. Parameter scans

The chosen scan parameters, which are all defined as scalar inputs to JETTO, are

(i) Greenwald density fraction $f_{\mathrm{GW}} = \langle n_{\mathrm{e}} \rangle_{\mathrm{line}}/n_{\mathrm{GW}}$,
(ii) normalised beta β_{N},
(iii) ECCD current drive efficiency ζ_{CD}
(iv) auxiliary power (P_{EC} and P_{EBW}),
(v) radiation fraction $f_{\mathrm{rad}} = P_{\mathrm{rad}}/P_{\mathrm{tot}}$.

Table 3 summarises the scan parameters and their ranges in each of the scans. All scan parameters span 21 equally spaced grid points, except for the scan in ζ_{CD}, which had six grid points. This totals to $21 \times 21 \times 3 + 21 \times 6 = 1\,449$ JETTO runs.

The scan parameters f_{GW} and β_{N} can be set to access a wide range of densities and temperatures, which are key parameters in the fusion power performance. As explained in sections 3.3 and 3.4, respectively, both parameters are defined as targets in feedback loops, with pellet fuelling rate and artificial rescaling of the anomalous diffusivity as control parameters, respectively. Effectively, varying β_{N} while keeping f_{GW} constant approximately varies the temperature while keeping the density constant, assuming small variation in the plasma current. This can be understood from the fact that $\beta_{\mathrm{N}} \propto \langle p \rangle / I_{\mathrm{p}} \sim \langle n \rangle \langle T \rangle / I_{\mathrm{p}} \propto \langle T \rangle f_{\mathrm{GW}}$ (n/T can be either electron or ion density/temperature in this context). Varying f_{GW} while keeping β_{N} constant at approximately constant current varies the density and temperature inversely. This way of accessing different temperature regimes using different transport assumptions rather than varying the auxiliary heating makes the confinement factor H_{98}^{*} a critical parameter for assessing the viability of the scenario. Considering that the O-X-B coupling scheme is sensitive to the density scale length $L_n = n/|\nabla n|$ [51], the EBW heating and current drive assumptions cannot be straightforwardly extrapolated from the EC+EBW template simulation in density and temperature space. For sufficient confidence in the EBW assumptions, the scan spaces should be restricted to the density and temperature ranges that have already been analysed with GENRAY/CQL3D (~ 10% variation). For this reason, a 2D scan in f_{GW} and β_{N} has been done for the EC template only, as presented in section 4.1.

The assessment of the confinement assumption is studied in more detail with the scan of section 4.2. Confinement scalings other than IPB98(y,2) are evaluated in a broad parameter space to compare the conclusions that they arrive at with regards to minimisation of the confinement factor. The scan spans the same space in Greenwald fraction f_{GW} as the one presented in section 4.1, with β_{N} fixed at 4.4, using the EC template. In addition, the JETTO definition of the EC current drive efficiency ζ_{CD} is scanned in order to access different current drive regimes.

Table 3. Scan parameters and ranges by section where the scan is presented. Numbers in bold are the scan variables of the particular scan.

Section	Template	$f_{\rm GW}$ [%]	$\beta_{\rm N}$ [ ]	$\zeta_{\rm CD}$	$P_{\rm EC}$ [MW]	$P_{\rm EBW}$ [MW]	$f_{\rm rad}$ [%]
4.1	EC	**50–120**	**4.2–5.5**	18.2	150	0	70
4.2	EC	**50–120**	4.4	**16–27**	150	0	70
4.3	EC+EBW	100	3.93	22.7	**2.5–90**	**42–140**	70
4.4	EC+EBW	100	3.93	22.7	9.0	**42–140**	**20–70**

Exploring the combined parameter space of $P_{\rm EC}$ and $P_{\rm EBW}$ is of interest because it efficiently varies the current and pressure peakings, with the EC and EBW absorption being on-axis and off-axis, respectively. Performing this scan while keeping the target $f_{\rm GW}$ and $\beta_{\rm N}$ fixed ensures little variation in average density and temperature, assuming a high bootstrap current fraction that keeps the total plasma current relatively constant, despite the auxiliary current drive varying significantly. At high auxiliary power, the anomalous heat diffusivity can be scaled up while maintaining the set target $\beta_{\rm N}$. If the corresponding reduction in energy confinement time $\tau_{\rm E}^*$ is larger than the reduction prescribed by the ITER scaling, $\tau_{98}^* \propto (P_{\rm net}^*)^{-0.69}$, the resulting confinement factor also decreases. A combined scan of $P_{\rm EC}$ and $P_{\rm EBW}$ for the EC+EBW template is presented in section 4.3.

Similarly to an increase of the auxiliary power, a reduction of the impurity radiation can potentially reduce the confinement factor. On the other hand, $P_{\rm sep}$ scales negatively with impurity radiation, meaning that low radiation fraction also increases $P_{\rm sep}/R_{\rm geo}$. In the scan presented in section 4.4, the combined $f_{\rm rad} = P_{\rm rad}/P_{\rm tot}$ and $P_{\rm EBW}$ space is explored, using the EC+EBW template.

4.1. Greenwald fraction and normalised beta

A full set of 2D plots of the estimated operational domains in the $f_{\rm GW}$,$\beta_{\rm N}$-space is shown in figure 7, where simulation outputs are compared against the individual limits listed in section 2.8 (figures 7(*a*)–(*g*)), as well as presenting the overlap of domains by counting number of satisfied operational criteria in each scan point (figures 7(*h*) and (*i*)). The two different overlap figures compare H_{98}^* against the conservative and the optimistic limit, respectively. Figure 8 shows the output from the same 2D scan sliced in a set of 1D plots at constant $\beta_{\rm N}$ (outputs are linearly interpolated in $\beta_{\rm N}$ where selected values do not fall exactly on a scan grid point).

The first observation to make is that the fusion power range $1.5\,{\rm GW} < P_{\rm fus} < 1.8\,{\rm GW}$ (see figures 7(*a*) and 8(*a*)) covers a narrow domain in $\beta_{\rm N}$, with the domain shifted towards higher $\beta_{\rm N}$ at low $f_{\rm GW}$. The temperature increases to some extent with increasing $\beta_{\rm N}$, but the increase is more substantial towards lower $f_{\rm GW}$ in the scan domain, with average ion temperature exceeding 25 keV at $f_{\rm GW} = 50\%$ (see figure 8(*j*)). However, at decreasing $f_{\rm GW}$ and constant $\beta_{\rm N}$, the increasing ion temperature is insufficient to balance the decreasing density for maintaining the total fusion power, which is why higher $\beta_{\rm N}$ is required at low $f_{\rm GW}$.

The criterion $Q_{\rm sci} > 11$ is only satisfied in a subdomain of the fusion power domain. The narrow band where both $Q_{\rm sci} > 11$ and $P_{\rm fus} < 1.8\,{\rm GW}$ can be identified from the green hues in the two overlap plots (figures 7(*h*) and (*i*)). The criterion $P_{\rm sep}/R_{\rm geo} < 45\,{\rm MW\,m^{-1}}$ has a limit that follows a similar shape to the $P_{\rm fus}$ and $Q_{\rm sci}$ limits in $f_{\rm GW}$,$\beta_{\rm N}$-space. The whole $P_{\rm fus}$ domain is contained in the $P_{\rm sep}/R_{\rm geo}$ domain, meaning that $P_{\rm sep}/R_{\rm geo} < 45\,{\rm MW\,m^{-1}}$ is redundant and not further restricting the operational space. However, the chance of detachment access generally increases with decreasing $P_{\rm sep}$. Figure 8(*e*) shows that $P_{\rm sep}/R_{\rm geo} \geqslant 40\,{\rm MW\,m^{-1}}$ in the $Q_{\rm sci} > 11$ domain. Such large $P_{\rm sep}/R_{\rm geo}$ might still pose a challenge for divertor design and detachment access.

An interesting feature is the non-monotonic dependency of the plasma current with respect to the Greenwald density fraction $f_{\rm GW}$, which is clearly seen in figure 8(*c*). This is because of opposing dependencies of the bootstrap current and the auxiliary current with respect to $f_{\rm GW}$ at constant $\beta_{\rm N}$. The EC current scales as $T_{\rm e}/n_{\rm e}$ according to equation (16), meaning that the EC current drive is expected to scale similarly to $f_{\rm GW}^{-2}$ ($\langle T_{\rm e}\rangle \sim \beta_{\rm N}/f_{\rm GW}$, $\langle n_{\rm e}\rangle \propto I_{\rm p} f_{\rm GW}$). This scaling is confirmed by the least square fit to the current drive, shown by the black dashed curve in figure 8(*h*). The increasing bootstrap current with increasing $f_{\rm GW}$ can be understood from the fact that the edge pressure gradient increases with increasing average density. It is possible that the fixed boundary density and temperatures contributes to this effect, and that it would become weaker with more self-consistent modelling of both the core and the SOL.

Similarly to the plasma current, there is a non-monotonicity of C_β with respect to $f_{\rm GW}$ at constant $\beta_{\rm N}$, which indicates that also the pressure peaking is non-monotonic (since C_β is a function of $\beta_{\rm N}$ and $F_p = p_{\rm ax}/\langle p\rangle$ only, see equation (4)). The reduction of pressure peaking at low Greenwald fraction can be understood from changes in the on-axis alpha particle component of the pressure as the ion temperature locally exceeds ~50 keV, with the details demonstrated in figure 9. Above these temperatures, the DT fusion cross section stops increasing significantly with ion temperature, meaning that it is unable to compensate for the decreasing density with decreasing Greenwald fraction to maintain on-axis fusion reaction rates. Unsurprisingly, C_β increases with increasing $\beta_{\rm N}$. Although the pressure peaking decreases slightly with $\beta_{\rm N}$ at constant $f_{\rm GW}$, this is not enough to compensate for the explicit $\beta_{\rm N}$ dependence in equation (4).

The conservative H_{98}^* criterion is only satisfied in the high-$f_{\rm GW}$, high-$\beta_{\rm N}$ corner of the scan space (figure 7(*g*)), which is beyond operational limits in $P_{\rm fus}$, $I_{\rm p}$ and $P_{\rm sep}/R_{\rm geo}$. In essence, this indicates that there are no operating points for a non-inductive scenario with sufficient fusion gain and realistic ECCD efficiency assumptions below $H_{98}^* = 1.2$. However,

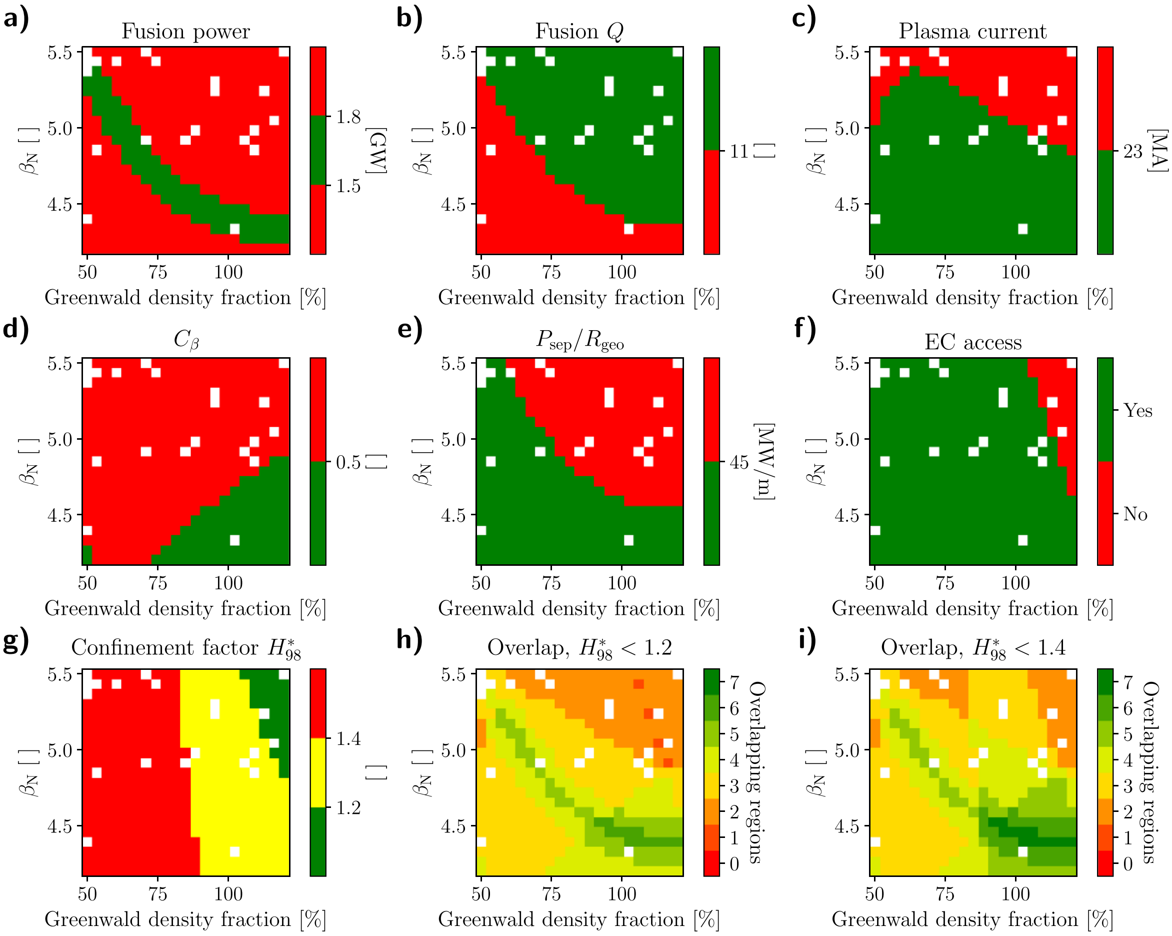

Figure 7. 2D scan in Greenwald density fraction and normalised beta, based on the EC template simulation. Figures (*a*)–(*g*) compares the outputs of all simulations against the listed operational limits in section 2.8, where green means that it operates within limits, and red means that the limit is exceeded. Figure (*g*) also shows in yellow the parameter space where the optimistic confinement limit is satisfied ($H^*_{98} \leqslant 1.4$), but not the conservative limit ($H^*_{98} \leqslant 1.2$). Figures (*h*) and (*i*) count the total number of operational limits satisfied, where figure (*h*) compares against the conservative confinement limit, and figure (*i*) compares against the optimistic limit. White dots correspond to gaps in the scan results due to simulations that did not converge for numerical reasons.

relaxing the confinement requirement to $H^*_{98} < 1.4$, a domain is found where all seven of the assumed operational limits are satisfied, shown with dark green in figure 7(*i*) ($f_{GW} \gtrsim 95\%$, $\beta_N \approx 4.4$). As mentioned in section 2.6, different confinement scalings suggest different density dependencies, where the IPB98(y,2) scaling has a relatively high positive density scaling with $\tau_{IPB98(y,2)} \propto \langle n_e \rangle^{0.41}$. Section 4.2 compares a slice of the presented scan results (β_N is fixed at 4.4) against a range of confinement scalings. The EC current drive efficiency ζ_{CD} is varied in addition to study its impact on confinement.

For different target values of f_{GW} and β_N, the confinement factor solution mostly varies with respect to f_{GW} (see figure 8(*f*)). In the high Greenwald fraction domain, the confinement factor decreases with respect to increasing β_N. This slightly counter-intuitive observation can be understood as a result of the non-inductive constraint. It can first be identified that

$$\tau^*_E = \frac{W_{th}}{P^*_{net}} \sim \frac{\langle p_{th} \rangle}{P^*_{net}} \sim \frac{I_p \beta_{N,th}}{P^*_{net}}, \quad \tau^*_{98} \sim I_p^{0.93} \langle n_e \rangle^{0.41} \left(P^*_{net}\right)^{-0.69}, \tag{20}$$

$$H^*_{98} = \frac{\tau^*_E}{\tau^*_{98}} \sim I_p^{0.07} \langle n_e \rangle^{-0.41} \left(P^*_{net}\right)^{-0.31} \beta_{N,th}$$
$$\sim I_p^{-0.34} f_{GW}^{-0.41} \left(P^*_{net}\right)^{-0.31} \beta_{N,th}, \tag{21}$$

where W_{th}, p_{th} and $\beta_{N,th}$ are the thermal stored energy, pressure and normalised β, respectively. P^*_{net} is the radiation corrected power (see details in section 2.6). Fixed field and geometry is assumed, with their dependencies consequently neglected in the derivations. By interpolating the scan data along $f_{GW} = 100\%$ and fitting each parameter $y \in \{I_p, P^*_{net}, \beta_{N,th}\}$ to a power law dependence in β_N according to $y \approx c_y \beta_N^{\alpha_y}$ yields the exponents $\alpha_I = 1.03$, $\alpha_P = 2.76$, and $\alpha_\beta = 0.90$. Under the modelling constraint, this gives that H^*_{98} has a total variation with respect to β_N according to $H^*_{98} \sim \beta_N^{\alpha_\beta - 0.34\alpha_I - 0.31\alpha_P} = \beta_N^{-0.30}$.

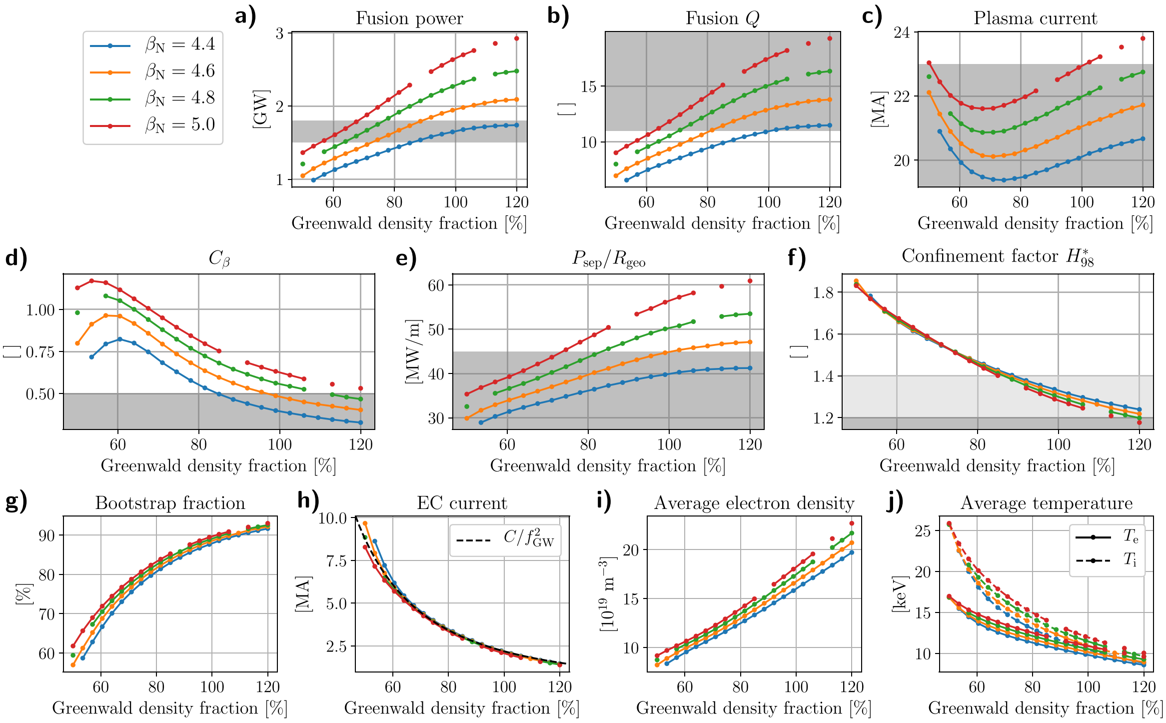

Figure 8. Simulation data from the scan in Greenwald density fraction f_{GW} and normalised beta β_N, sliced at selected constant β_N values. The figures (*a*)–(*f*) present the output parameters that are compared against the set operational limits, with the operational domain of each output highlighted in grey. Figure (*f*) categorises two different operational limits for H^*_{98}: The conservative limit $H^*_{98} < 1.2$ shown in dark grey, and the optimistic limit $1.2 \leqslant H^*_{98} < 1.4$ shown in light grey. Additional simulation output is shown in figures (*g*)–(*j*).

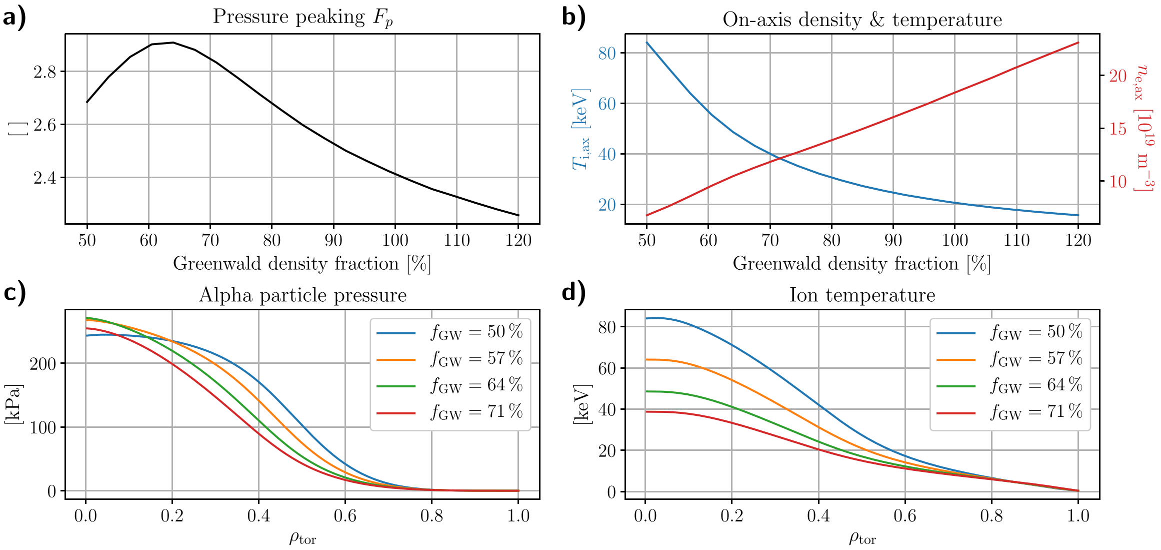

Figure 9. Data from the scan in f_{GW} and β_N at $\beta_N = 4.2$.

A corresponding analysis of the H^*_{98} solution by varying the Greenwald fraction f_{GW} and keeping β_N constant is challenging, since neither of the parameters I_p, P^*_{net}, and $\beta_{N,th}$ follow simple power law dependencies with respect to f_{GW} at constant β_N. However, making a power law fit to $H^*_{98}(f_{GW})$ directly at $\beta_N = 4.4$ yields an overall exponent $\alpha_f = -0.42 \approx -0.41$, indicating that $I_p^{-0.34}(P^*_{net})^{-0.31}\beta_{N,th}$ is largely a function of β_N under the modelling constraints, independent of f_{GW}.

The estimated domain of access to the 2nd harmonic O-mode for EC heating and current drive is shown in figure 7(*f*), based on $n_{e,ax}$ and B_{ax} at each scan point. Since B_{geo} is held fixed in the scan, the on-axis magnetic field strength B_{ax} only varies with the Shafranov shift. On the other hand, the density covers a wide range in the scan, as indicated by figure 8(*i*). It is only in the high-density corner of the scan space (high Greenwald fraction and high β_N) that the on-axis density exceeds the cut-off density. However, this domain is already outside of the operational limits in fusion power, plasma current and $P_{\mathrm{sep}}/R_{\mathrm{geo}}$. Hence, EC coupling access does not restrict the overall operational regime.

4.2. Greenwald fraction and normalised ECCD efficiency

No empirical confinement scaling has a validity domain that includes STEP relevant regimes, since there have never been any experiments of similar scale. The confinement in the scans is mainly assessed by comparing the IPB98(y,2) (radiation-corrected) confinement factor against a set of fixed upper limits. In order for the IPB98(y,2) confinement factor to accurately quantify the degree of over-/under-estimation of the confinement, the confinement time must have similar dependencies with respect to current, density and power around the STEP operating points as those suggested by $\tau^{*}_{\mathrm{IPB98(y,2)}} \propto I_{\mathrm{p}}^{0.93} \langle n_{\mathrm{e}} \rangle^{0.41} (P^{*}_{\mathrm{net}})^{-0.69}$. The main argument in favour of using IPB98(y,2) for this purpose compared to other empirical scalings is that it is based on H-mode data for a relatively large set of experiments.

As seen in figure 8(*f*), the IPB98(y,2) scaling indicates that a high Greenwald fraction minimises the confinement factor, which makes operating points in that regime to appear the most realistic from a confinement assumption perspective. In this subsection, a range of alternative confinement factor scalings are evaluated for a 1D slice of the scan of section 4.1 (at $\beta_{\mathrm{N}} = 4.4$) in order to test the hypothesis that a high Greenwald fraction is preferable irrespective of the confinement scaling to compare against. In conjunction, the normalised ECCD current drive efficiency ζ_{CD} is scanned to study how different ζ_{CD} assumptions perturbs the domains of minimum confinement. Scanning ζ_{CD} effectively varies the plasma current I_{p}, which is also a parameter that has a wide range of suggested dependencies according to different empirical scalings.

Figures 10(*a*)–(*f*) evaluate the confinement factor according to the IPB98(y,2) [8], ITPA20 [74], ITPA20−IL [74], Petty08 [73], NSTX(19) [10], and Kurskiev [102] scalings for the scan in f_{GW} and ζ_{CD}, and figures 10(*g*)–(*k*) show the input parameters for the scalings that vary across the scan. Table 4 lists the exponents for each of the six presented confinement scalings. For consistency, radiation is not taken into account, since the correction for highly core-radiating plasmas has only been derived for the IPB98(y,2) scaling [15]. Most scalings predict a monotonically decreasing confinement with increasing Greenwald fraction. One exception is the NSTX(19) scaling, which has a minimum around $f_{\mathrm{GW}} = 90\%$. This is because of the negative density scaling ($\tau_{\mathrm{NSTX(19)}} \propto \langle n_{\mathrm{e}} \rangle^{-0.05}$), which together with the negative power scaling causes a net increase of the confinement factor for $f_{\mathrm{GW}} \gtrsim 90\%$. The ITPA20-IL scaling also shows non-monotonicity of the confinement factor with respect to f_{GW} at high ECCD efficiency. The relatively strong current dependency of $\tau_{\mathrm{ITPA20-IL}} \propto I_{\mathrm{p}}^{1.291}$ decreases the confinement factor as the ECCD current increases at low f_{GW}, high ζ_{CD}. As will be seen in section 5, a high-density flat-top point ($f_{\mathrm{GW}} \sim 100\%$) has been derived as a potential candidate for the EC only scenario, which is partly based on the results indicated by the IPB98(y,2) scaling. A low-density candidate point is suggested as an alternative, which considers results from other confinement scalings (in particular ITPA20-IL).

It can be observed that the dependence of the scaling factors with respect to the current drive efficiency ζ_{CD} diminishes in the limit of high Greenwald density fractions. This is because the bootstrap fraction becomes larger in this limit (see figure 8(*g*)), and the total plasma current consequently becomes less sensitive to the ECCD assumptions. Similarly, the other variable parameters of the scaling laws, i.e. $\langle n_{\mathrm{e}} \rangle$ and P_{net}, also become less dependent on ζ_{CD} (see figures 10(*g*)–(*i*)).

4.3. EBW and EC power

The results of the scan in EC and EBW power space are shown in figures 11 and 12. The EBW system, which has off-axis heating and current drive, is generally more efficient than EC for driving current. This is supported by the observations in figures 11(*c*) and 12(*c*). The fusion power also increases significantly more with respect to EBW power than EC power, even though the on-axis EC heating couples directly to the core, where the fusion power density usually peaks. However, the target Greenwald density fraction in the fuelling rate feedback is kept fixed at 100%, meaning that the average density scales with the total plasma current. It can be observed in figure 12(*i*) that the average density indeed increases with the EBW power, which in turn contributes to the increase of fusion power. The fact that the target β_{N} also remains fixed causes the average temperature to be relatively constant throughout the auxiliary power scan space, as seen in figure 12(*j*). Unsurprisingly, the fusion Q is the highest in the low auxiliary power corner of the scan.

Comparing the $Q > 11$ domain of figure 11(*b*) against the curves of constant auxiliary power in figure 11(*a*), EBW heating appears to be preferable over EC heating for high fusion Q. β_{N} is held fixed throughout the scan at a value of 3.93, which is marginally above the estimated no-wall β_{N} limit of 3.7. C_{β} only exceeds 0.5 for two scan points in the low EBW power, high EC power corner of the scan space, where the pressure peaking is large and the RWM ideal-wall limit is low in β_{N}. The main disadvantages of EBW heating and current drive compared to EC, as observed from the operational domains in figure 11, are the relatively higher $P_{\mathrm{sep}}/R_{\mathrm{geo}}$ along the curves of constant auxiliary power (figure 11(*e*)), and the more efficient current drive risking to exceed total current limits (figure 11(*c*)). However, in the auxiliary power scan space, there is a wide region where both $P_{\mathrm{sep}}/R_{\mathrm{geo}}$ and I_{p} are well within operational limits.

The confinement factor H^{*}_{98} is the lowest in the regimes of high auxiliary power, which follows from the fact that high heating power can maintain the temperature regime prescribed by the f_{GW}, β_{N} combination at low energy confinement time. This reduction of confinement time is larger than the reduction suggested by the $\tau_{\mathrm{IPB98(y,2)}}$ scaling. Similarly, high auxiliary current drive (primarily with EBW) tends to reduce the confinement time relative to $\tau_{\mathrm{IPB98(y,2)}} \propto I_{\mathrm{p}}^{0.93}$. Domains where

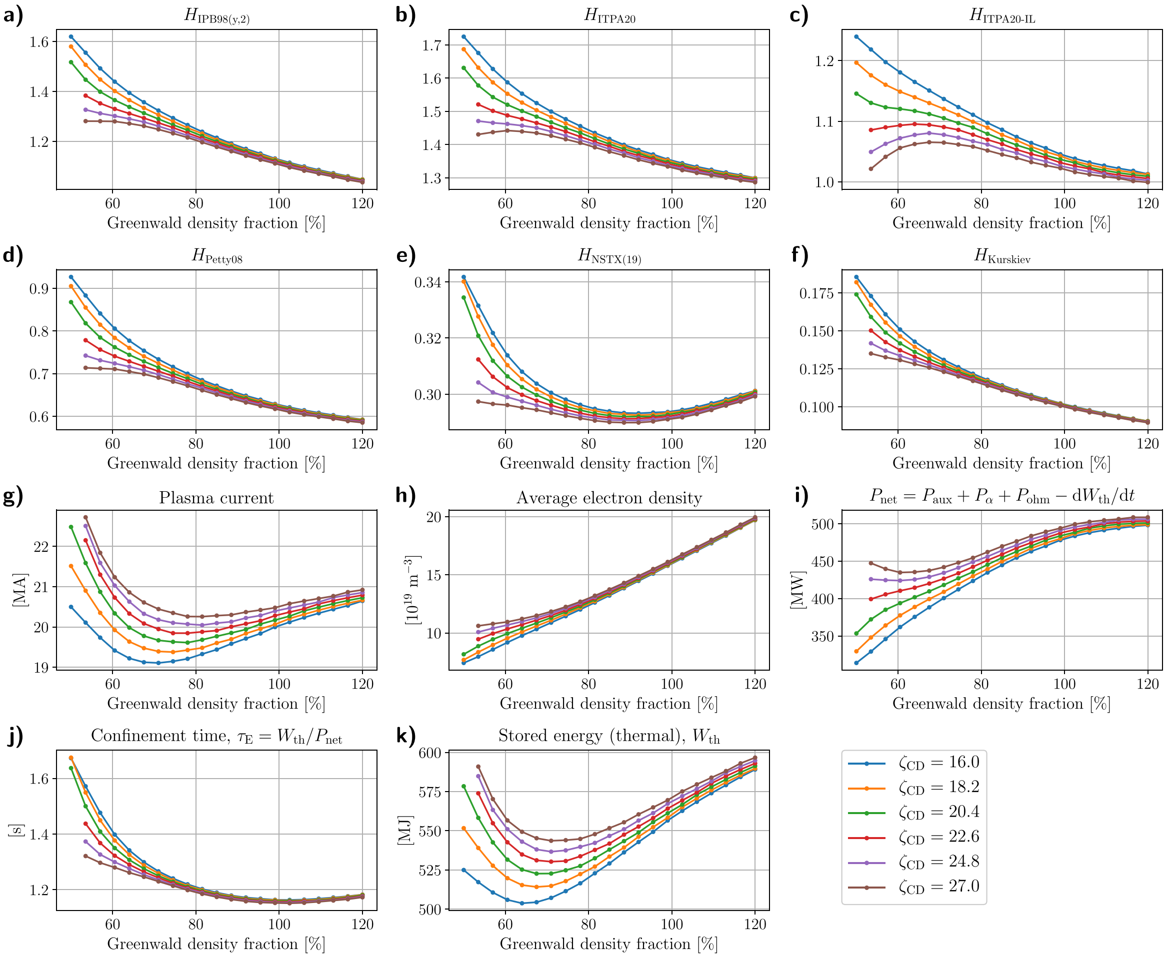

Figure 10. Confinement factors evaluated using a range of different empirical scalings, based on a 2D scan in Greenwald fraction f_{GW} and normalised ECCD efficiency ζ_{CD} (see definition in equation (16)) using the EC only scan template.

Table 4. Exponents for the plasma current, line averaged density and net power according to the confinement scalings presented in figure 10.

	IPB98(y,2)	ITPA20	ITPA20-IL	Petty08	NSTX(19)	Kurskiev
I_{p}	0.93	0.976	1.291	0.75	0.54	0.53
$\langle n_{\mathrm{e}} \rangle$	0.41	0.2442	0.1473	0.32	−0.05	0.65
P_{net}	−0.69	−0.6687	−0.6442	−0.47	−0.38	−0.58

the conservative confinement assumption is satisfied can be found for auxiliary powers above 113.1 MW in the scan space, with a preference for high EBW power over high EC power along curves of constant auxiliary power. There is a relatively wide region in the scan space where all seven operational limits are satisfied, including the conservative confinement assumption, as seen in figure 11(*h*). With the optimistic assumption in figure 11(*i*), the fully compliant operating space is no longer limited by high H^*_{98}, but rather by $P_{\mathrm{fus}} > 1.5$ GW (for $P_{\mathrm{EBW}} \lesssim 80$ MW). Increasing β_{N} can potentially bring the operating point above the fusion power lower limit while satisfying the optimistic confinement assumption at low auxiliary power, suggesting the existence of a high fusion Q operating point in the EC+EBW flat-top scenario. Out of all scan points in the four parameter scans, the point in the low auxiliary power corner of the scan in P_{EC} and P_{EBW} demonstrated the lowest value of $P_{\mathrm{sep}} - P_{\mathrm{L-H}}$, following the $P_{\mathrm{L-H}}$ definition of equation (15). The obtained value at this point, $P_{\mathrm{sep}} - P_{\mathrm{L-H}} = 89.3$ MW, is well within the positive range, meaning that all presented scan points indicate H-mode confinement.

Access to both EC and EBW heating and current drive is estimated in figure 11(*f*). Red coloured domains would indicate that at least one of the two auxiliary systems lacks access. With neither the density nor the on-axis magnetic field varying significantly from the values at the EC + EBW scan template, which has confirmed EC and EBW access, there is no part of the scan space where the electron gyro-frequency falls outside any of the coupling domains.

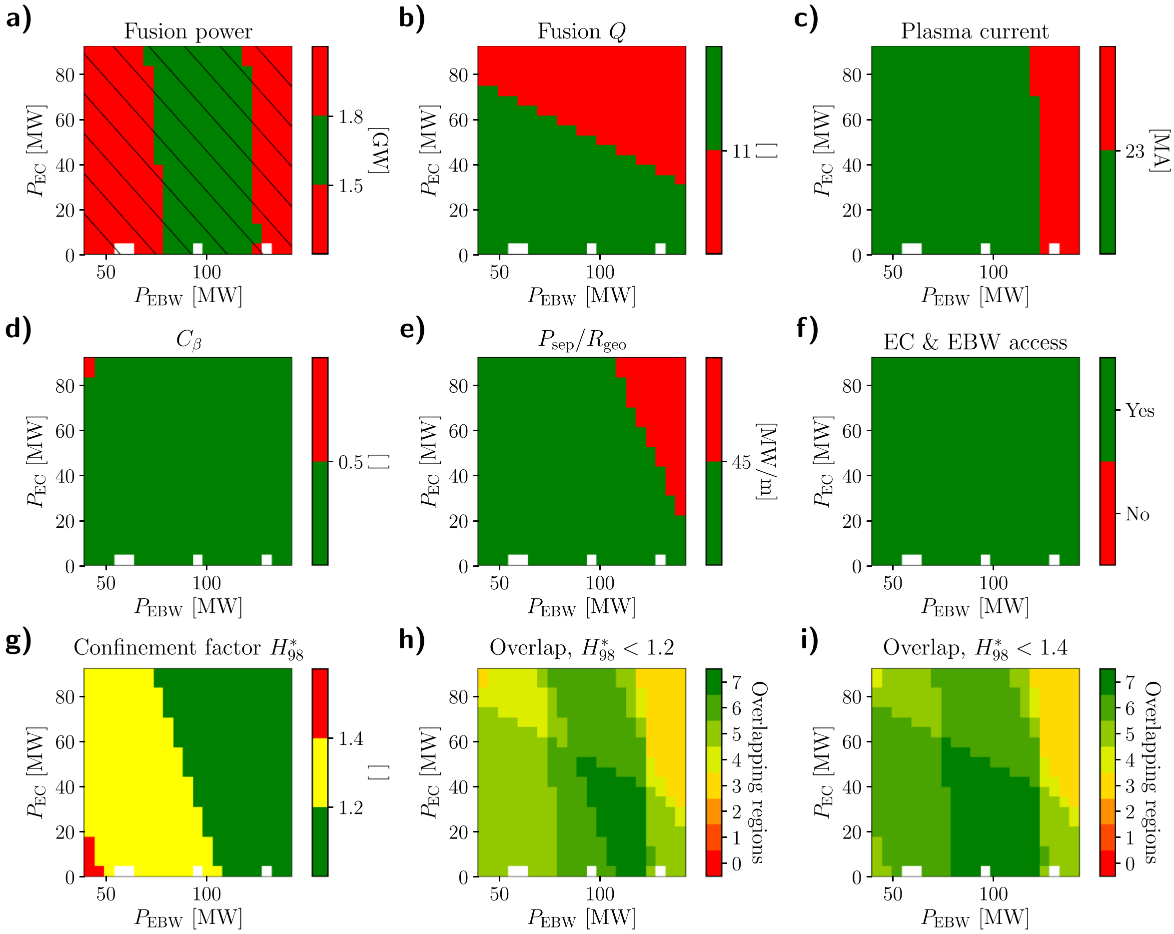

Figure 11. 2D scan in EC and EBW auxiliary power, based on the EC+EBW template simulation. Figures (*a*)–(*g*) compares the outputs of all simulations against the listed operational limits in section 2.8, where green means that it operates within limits, and red means that the limit is exceeded. The black lines in figure (*a*) correspond to curves of constant auxiliary power. Figure (*g*) shows in yellow the parameter space where the optimistic confinement limit is satisfied ($H_{98}^* \leqslant 1.4$), but not the conservative limit ($H_{98}^* \leqslant 1.2$). Figures (*h*) and (*i*) count the total number of operational limits satisfied, where figure (*h*) compares against the conservative limit, and figure (*i*) compares against the optimistic limit.

4.4. EBW power and radiation fraction

The results from the scan varying the EBW power and radiation fraction are presented in figures 13 and 14. Radiation fraction is not varied self-consistently with core impurity content in this scan. Rather, the core radiation is prescribed, with a flat profile in radiation power density for simplicity (see details of the impurity and radiation assumptions in section 3.7). Since the target Greenwald density fraction and the normalised β are both kept constant, the average temperatures remain approximately constant in the whole scan space. A reduction of the radiation fraction results in increased transport and lower H_{98}^*. Since variation of the radiation fraction also does not influence the plasma current considerably, as seen in figure 14(*c*), the density also remain relatively unchanged along this scan dimension. For this reason, the fusion power and fusion Q do not depend on the radiation fraction, as demonstrated in figures 14(*a*) and (*b*).

Similarly to the scan of section 4.3, β_{N} is fixed at $\beta_{\mathrm{N}} = 3.93$, which is close to the estimated RWM no-wall limit. With the EC power being fixed at 9.0 MW, the pressure peaking never gets large enough to significantly reduce the ideal-wall limit and push C_β above 0.5. Also, neither the on-axis electron density nor the magnetic field vary significantly in the scan space (see figures 14(*i*) and (*j*)), meaning that EC and EBW are both likely to be accessible in the whole scan domain, as indicated by figure 13(*f*).

The domain where all seven operational limits are satisfied, including the conservative confinement assumption, is primarily limited by $P_{\mathrm{sep}}/R_{\mathrm{geo}}$ and H_{98}^*, which can be seen in figures 13(*e*), (*g*) and (*h*). With the optimistic confinement assumption, the operational domain is limited in the low end of P_{EBW} by $P_{\mathrm{fus}} > 1.5$ GW. Due to the $P_{\mathrm{sep}}/R_{\mathrm{geo}} < 45\,\mathrm{MW\,m^{-1}}$ limit, the radiation fraction cannot drop below 60% while still satisfying either the fusion power limitation or the conservative confinement assumption. Increasing β_{N} for expanding the fusion power limit in the low EBW power domain is unlikely to expand the operational radiation fraction domain, since increasing β_{N} also increases $P_{\mathrm{sep}}/R_{\mathrm{geo}}$ (see figure 8(*e*)).

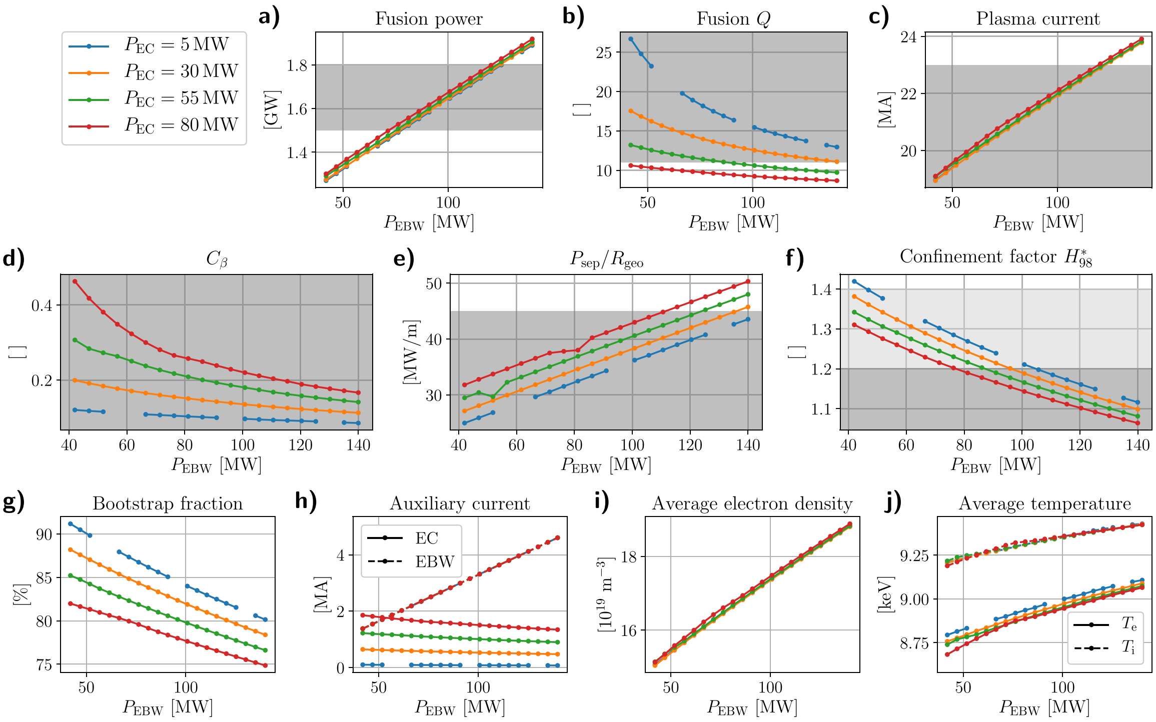

Figure 12. Simulation data from the scan in EC and EBW auxiliary power, sliced at selected constant P_{EC} values. The figures (*a*)–(*f*) present the output parameters that are compared against the set operational limits, with the operational domain of each output highlighted in grey. Figure (*f*) categorises two different operational limits for H^*_{98}: the conservative limit $H^*_{98} < 1.2$ shown in dark grey, and the optimistic limit $1.2 \leqslant H^*_{98} < 1.4$ shown in light grey. Additional simulation output is shown in figures (*g*)–(*j*).

5. Candidate operational points

The analysis provided by the scans suggests at least four candidate flat-top points, depending on the confinement assumptions: two EC only and two EC+EBW operational points. The EC only scenario suggests $\beta_{\mathrm{N}} \approx 4.5$ and $f_{\mathrm{GW}} \approx 100\%$ with $H^*_{98} < 1.4$. The operational domain does not expand when ignoring the $H^*_{98} < 1.4$ requirement because of the assumed limit $C_\beta < 0.5$ (see figure 7(*d*)), which implies the restriction $f_{\mathrm{GW}} \gtrsim 85\%$ along the narrow $P_{\mathrm{fus}} < 1.8\,\mathrm{GW}$, $Q_{\mathrm{sci}} > 11$ domain. However, interpreting the estimated $C_\beta < 0.5$ as a soft limit (see discussions in section 2.4 for details), lower density regimes can be explored by reducing f_{GW} while increasing β_{N} along the narrow domain where the limits on fusion power and fusion Q are both satisfied. As discussed in section 4.2, some scalings predict minimum confinement in lower density regimes ($f_{\mathrm{GW}} \lesssim 90\%$), meaning that there is a chance that these regimes are more accessible from a confinement point of view, supposing that any of these scalings are more valid than IPB98(y,2) in STEP relevant regimes. The two flat-top point categories of the EC only scenario are here labelled EC-HD [103] and EC-LD [104] (for high density and low density, respectively). As discussed in section 4.3, the EC+EBW scenario suggests a domain of relatively high EBW power ($P_{\mathrm{EBW}} \gtrsim 100\,\mathrm{MW}$) when $H^*_{98} < 1.2$. Significantly lower P_{aux} and higher Q_{sci} domains can in principle be accessed if β_{N} is increased (to expand the domain with $P_{\mathrm{fus}} > 1.5\,\mathrm{GW}$ to lower P_{EBW}) while relaxing the H^*_{98} limit. Two flat-top point categories for the EC+EBW scenario are here labelled as EB-CC [105] (CC: conservative confinement) and EB-HQ [106] (HQ: high fusion Q).

Higher fidelity JETTO modelling has explored these four operational points with more realistic physics assumptions compared to those of the scans in section 4. Rather than prescribing the radiation fraction, impurity radiation is self-consistently predicted with atomic physics from SANCO [101] combined with impurity transport from JETTO (the transport assumptions are still based on NCLASS and rescaled Bohm/gyro-Bohm, as described in section 3.3). The seeded radiating impurity species are xenon and argon, with argon primarily being used for divertor conditioning using gas puffing, whereas xenon is seeded with doped fuelling pellets to bring the core radiation to the required level for detachment access (see details in section 2.7). The criteria for the optimisation of the q-profile shaping have also been refined when developing the candidate flat-top points compared to the template simulations (see [64] for a full list of criteria). A summary of 0D outputs from the higher fidelity simulations are presented in table 5, and profile data for the four scenarios are presented in figure 16. With the radiation distribution self-consistently calculated from core impurities, this is taken into account when calculating the H^*_{98} confinement factor. Each operating point has been further analysed with MHD code MARS-F for assessing RWM stability. Values for $\beta_{\mathrm{N}}^{\mathrm{no-wall}}$ and $\beta_{\mathrm{N}}^{\mathrm{ideal-wall}}$ have been computed with the code, rather than using the values that were used in the analysis of the scan results. The results are presented in table 7; it should be noted that further profile optimisation to raise these β-limits could be possible.

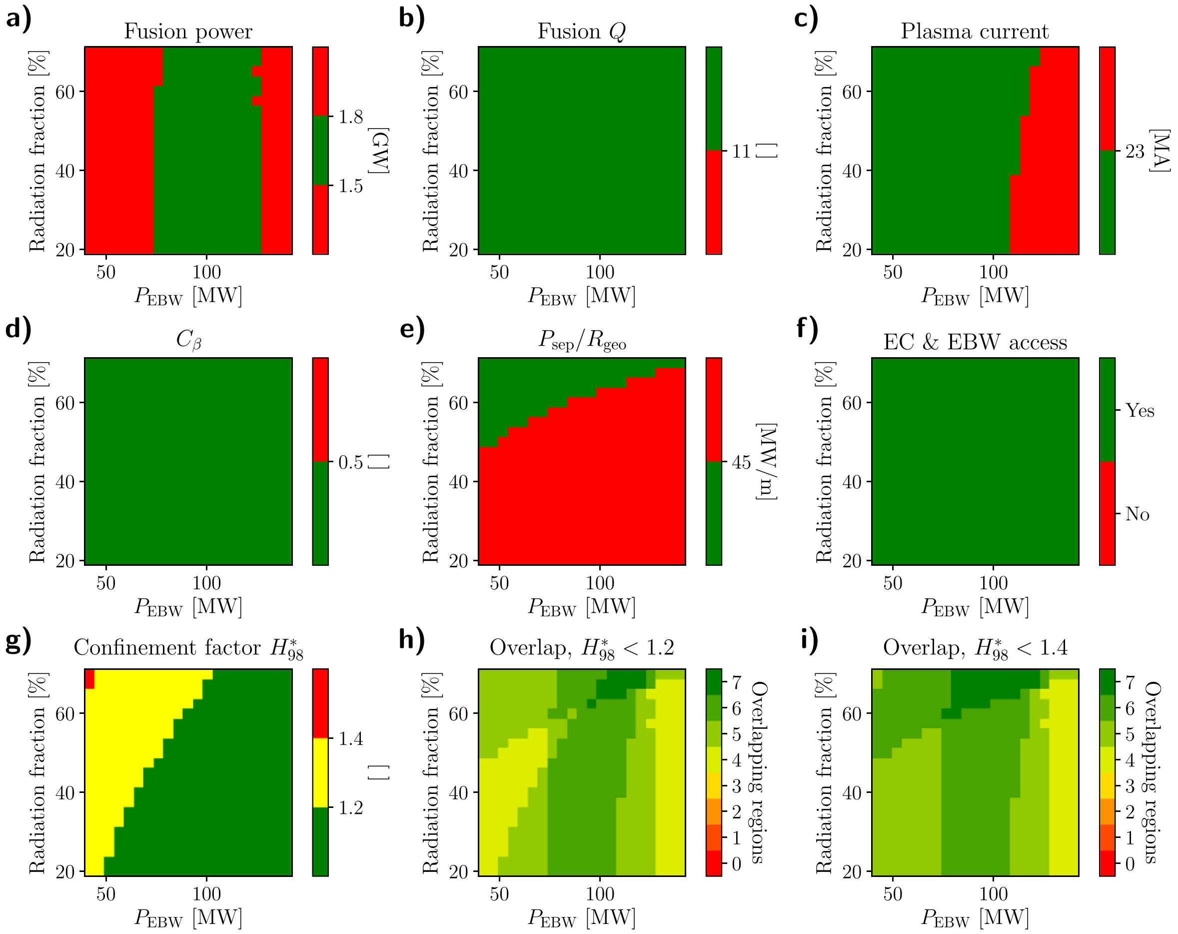

Figure 13. 2D scan in EBW power and radiation fraction, based on the EC+EBW template simulation. Figures (*a*)–(*g*) compares the outputs of all simulations against the listed operational limits in section 2.8, where green means that it operates within limits, and red means that the limit is exceeded. Figure (*g*) shows in yellow the parameter space where the optimistic confinement limit is satisfied ($H^*_{98} \leqslant 1.4$), but not the conservative limit ($H^*_{98} \leqslant 1.2$). Figures (*h*) and (*i*) count the total number of operational limits satisfied, where figure (*h*) compares against the conservative limit, and figure (*i*) compares against the optimistic limit.

The operational points are placed on top of the overlap plots for the scans of sections 4.1, 4.3 and 4.4 in figure 15, to indicate where the points are in relation to the operational spaces of the scans. The impact of impurities on the plasma properties, as well as the self-consistent recalculation of the auxiliary heating and current drive efficiencies at the candidate operational points, mean that the points do not exactly match the corresponding locations in the scans. Dilution by impurities is slightly higher in the candidate flat-top points compared to the scan data, meaning that the fusion power and fusion Q are generally lower than predicted by the scans. The higher degree of dilution can most easily be seen in figure 16(*k*), with the D + T concentration ranging between 58 and 73% on-axis. This can be compared against the D + T concentration in the scans, which was set to $c_{\mathrm{D+T}} = 1 - 2c_{\mathrm{He}} - 54c_{\mathrm{Xe}} = 79.6\%$. The EC auxiliary powers also differ for the EC-LD and the EB-HQ points relative to the scan templates used in the (f_{GW}, β_{N}) and the ($P_{\mathrm{EBW}}, f_{\mathrm{rad}}$) scans, respectively.

EC-HD satisfies all the listed operational limits except for $C_\beta < 0.5$, assuming that the optimistic confinement assumption is valid. The C_β limit is only marginally exceeded at $C_\beta = 0.54$, and it is possible that RWM control is still manageable with a combination of induced rotation and external control coils, as discussed in section 2.4. As indicated by figure 8(*d*), C_β can be reduced either by reducing β_{N} or by increasing f_{GW}. It is likely that a reduction of β_{N} will also reduce Q_{sci} below 11. An increased Greenwald fraction might also reduce the required degree of confinement, as indicated by figures 10(*a*)–(*f*) ($H_{\mathrm{NSTX(19)}}$ is the only exception). As discussed in section 2.4, operation at densities above the Greenwald limit has been demonstrated in scenarios with low ELM activity [69]. Whether these regimes are applicable to STEP without significant risk of disruption events remains to be analysed.

The low density EC operational point is out of range with respect to the suggested operational limit in Q_{sci}, with $Q_{\mathrm{sci}} = 9.22 < 11$. In addition, the EC-LD point has a plasma current $I_{\mathrm{p}} = 25.11\,\mathrm{MA} > I_{\mathrm{p,max}} = 25\,\mathrm{MA}$ (the limit of 23 MA was assumed for the scans only, see discussion in section 2.5), and $C_\beta = 0.60 > C_{\beta,\mathrm{max}} = 0.5$. The scan of section 4.1 (scan parameters f_{GW} and β_{N} in EC only scenario) indicates that the most efficient ways to increase Q_{sci} is to either increase β_{N} or

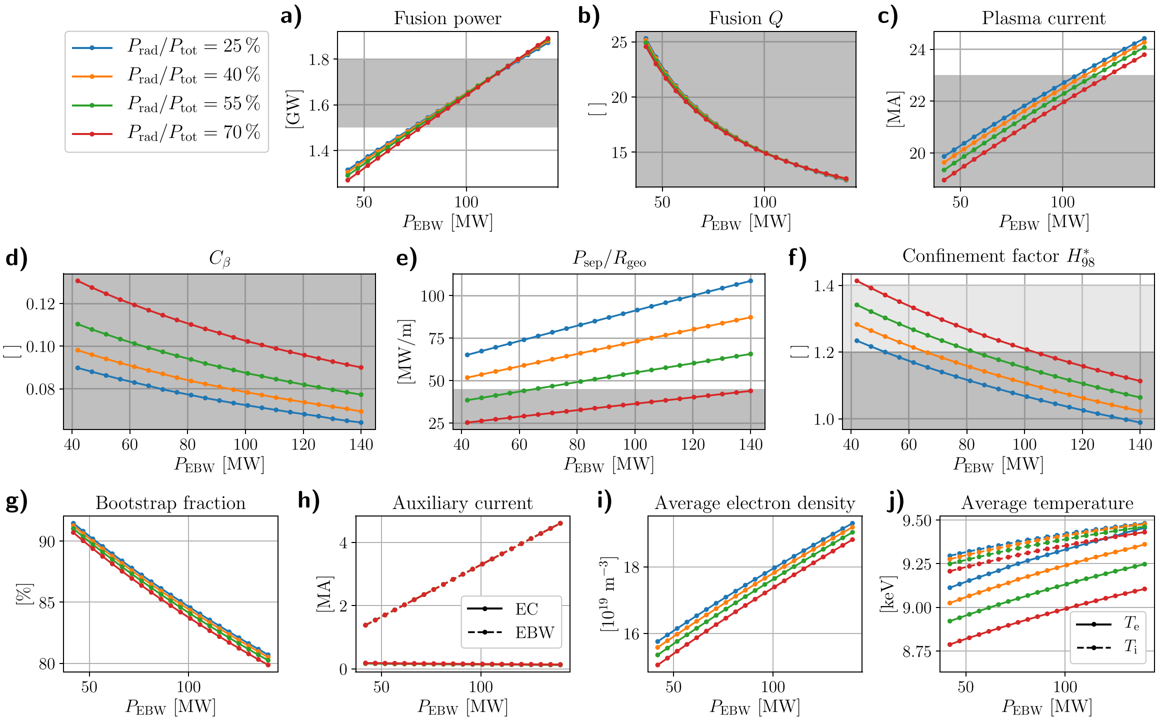

Figure 14. Simulation data from the scan in EBW power and radiation fraction, sliced at selected constant $f_{\rm rad} = P_{\rm rad}/P_{\rm tot}$ values. The figures (*a*)–(*f*) present the output parameters that are compared against the set operational limits, with the operational domain of each output highlighted in grey. Figure (*f*) categorises two different operational limits for H^*_{98}: The conservative limit $H^*_{98} < 1.2$ shown in dark grey, and the optimistic limit $1.2 \leqslant H^*_{98} < 1.4$ shown in light grey. Additional simulation output is shown in figures (*g*)–(*j*).

$f_{\rm GW}$. Increasing $\beta_{\rm N}$ only is likely not to access an operational point, as there is a positive trend of $I_{\rm p}$ with respect to $\beta_{\rm N}$, and $I_{\rm p}$ of EC-LD already exceeds the suggested limit of 25 MA. Increasing the Greenwald density fraction could potentially decrease $I_{\rm p}$ due to the non-monotonic dependency of $I_{\rm p}$ with respect to $f_{\rm GW}$ (see figure 8(*c*)). However, the minimum of $I_{\rm p}$ in that dependency is expected to be close to the EC-LD point ($f_{\rm GW} = 61.23\%$, $\beta_{\rm N} = 5.10$), meaning that a significant decrease of $I_{\rm p}$ is not expected. A combination of increased $f_{\rm GW}$ and decreased $\beta_{\rm N}$ is likely required to access an operational point relative to EC-LD in terms of $Q_{\rm sci}$ and $I_{\rm p}$. Moving in this direction in parameter space is also likely to reduce C_β, as indicated by figure 8(*d*). An issue with the high on-axis current density from ECCD in the EC-LD point is that $q_{\rm min} = 2.15$ is below the recommended lower limit of 2.2 (highlighted in red in the table). Simply reducing the EC power is not viable since it would decrease the fusion power, which is already close to the lower limit of 1.5 GW.

One of the main motivations for the low-density EC operating point was to minimise the confinement according to empirical scalings different from IPB98(y,2). However, as seen in table 6, all of the listed confinement factors predict the highest value for the EC-LD point, including the $H_{\rm ITPA20-IL}$ scaling. It is possible that $H_{\rm ITPA20-IL}$ can be reduced by increasing the plasma current, due to its relatively strong dependence in $\tau_{\rm ITPA20-IL} \propto I_{\rm p}^{1.291}$. However, this is not an option due to the current already exceeding tolerable levels, as outlined in the paragraph above. In addition to the confinement factors, table 6 also presents data on the pellet fuelling rate $S_{\rm pel}$, the fusion burn-up fraction $f_{\rm BU} = S_\alpha/S_{\rm pel}$, and the particle confinement time $\tau_{\rm p} = V\langle n_{\rm e}\rangle/S_{\rm pel}$. With the relatively low pellet fuelling rate of the EC-LD point, the burn-up fraction and the particle confinement time become unphysically large (of the orders 1000% and 1000 s, respectively). In appendix, the particle confinement assumption has been assessed in more detail for the EC-LD point. It was demonstrated that the empirical pinch velocity term of equation (12) had a significant impact on the particle confinement, and removing the term altogether increased the fuelling rate by a factor ~40 and gives more realistic burn-up fractions. However, the resulting scenario also had a reduced $q_{\rm min}$, which might trigger MHD instabilities such as NTMs and sawteeth, and a higher $P_{\rm sep}/R_{\rm geo}$, which poses challenges to the detachment access. It is evident that more work is needed to develop a potentially viable alternative for the EC scenario in the low-density regime.

The most promising operational point of the four candidates is EB-CC, which operates within all of the suggested limits, including the conservative confinement assumption $H^*_{98} < 1.2$. As discussed in section 2.3, the main caveat of the EC+EBW scenario is the assumption of the high current drive efficiency of EBW, which has little experimental verification. The EB-HQ point is significantly closer to reactor relevant conditions, with $Q_{\rm sci} = 29.07$. The relatively low $P_{\rm sep}/R_{\rm geo} = 34.87\ {\rm MW\,m^{-1}}$ also means that detachment access is expected to be easier compared to the other candidate flat-top points. The lower $P_{\rm sep}/R_{\rm geo}$ also results in the lowest value of $P_{\rm sep} - P_{\rm L-H}$. However, it is still positive with a large margin, indicating that H-mode access is likely for all four operating points.

Table 5. Summary of 0D outputs from the candidate operational points. The top six rows show the outputs relative to defined operational limits indicated by colour, using the same colourmap as the 2D plots of section 4 (see e.g. figures 13(*a*)–(*e*) and (*g*)). $P_{\mathrm{L-H}}$ is computed using equation (15). Complementary data on confinement, fuelling and burn-up is presented in table 6.

		EC-HD	EC-LD	EB-CC	EB-HQ
P_{fus}	[GW]	**1.68**	**1.51**	**1.56**	**1.62**
Q_{sci}	[ ]	**11.1**	**9.22**	**12.0**	**29.1**
I_{p}	[MA]	**21.2**	**25.1**	**22.7**	**21.3**
$C_\beta{}^*$	[ ]	**0.54**	**0.60**	**0.11**	**0.27**
$P_{\mathrm{sep}}/R_{\mathrm{geo}}$	[MW m^{-1}]	**39.0**	**40.1**	**39.9**	**34.9**
H^*_{98}	[ ]	**1.35**	**1.62**	**1.19**	**1.36**
P_{EC}	[MW]	150	160	9.00	6.30
P_{EBW}	[MW]	—	—	120	48.2
P_{rad}	[MW]	343	321	297	252
$P_{\mathrm{sep}} - P_{\mathrm{L-H}}$	[MW]	98.6	110	99.3	84.0
$\langle n_{\mathrm{e}} \rangle$	[10^{19} m^{-3}]	15.1	11.6	16.4	15.6
$\langle n_{\mathrm{e}} \rangle_{\mathrm{line}}/n_{\mathrm{GW}}$	[%]	94.8	61.2	96.4	97.8
$\langle T_{\mathrm{e}} \rangle$	[keV]	11.0	18.1	9.69	10.1
$\langle T_{\mathrm{i}} \rangle / \langle T_{\mathrm{e}} \rangle$	[ ]	1.07	1.24	1.04	1.06
$I_{\mathrm{BS}}/I_{\mathrm{p}}$	[%]	89.5	81.1	81.2	89.7
I_{EC}	[MA]	1.87	4.22	0.155	0.126
I_{EBW}	[MA]	—	—	3.95	1.70
$I_{\mathrm{EC}}/P_{\mathrm{EC}}$	[kA MW^{-1}]	12.5	26.4	17.2	20.0
$I_{\mathrm{EBW}}/P_{\mathrm{EBW}}$	[kA MW^{-1}]	—	—	32.9	35.2
$I_{\mathrm{aux}}/P_{\mathrm{aux}}$	[kA MW^{-1}]	12.5	26.4	31.8	33.4
β_{N}	[%]	4.50	5.10	3.93	4.30
β_{tor}	[%]	15.0	20.0	13.9	14.3
B_{axis}	[T]	2.46	2.46	2.45	2.36
l_{i}	[ ]	0.491	0.529	0.419	0.459
$l_{\mathrm{i}}(3)$	[ ]	0.275	0.296	0.234	0.257
q_{min}	[ ]	2.50	**2.15**	2.56	2.42
q_{95}	[ ]	9.07	7.93	8.03	8.84
Z_{eff}	[ ]	2.72	4.58	2.31	2.43

$^*C_\beta$ is evaluated using values of $\beta_{\mathrm{N}}^{\mathrm{no-wall}}$ and $\beta_{\mathrm{N}}^{\mathrm{ideal-wall}}$ predicted by MARS-F [36] for each individual operating point, see details of table 7.

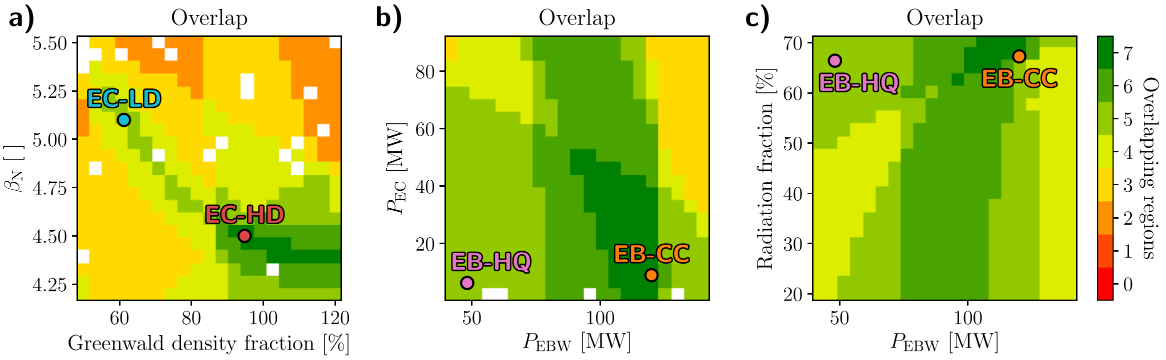

Figure 15. The location of the four candidate flat-top operational points in the scans of sections 4.1, 4.3 and 4.4. The overlap plots of figures (*a*), (*b*) and (*c*) correspond to figures 7(*i*), 11(*h*) and 13(*h*), respectively. The two EC only operational points, EC-HD and EC-LD, are placed in the EC only scan (figure (*a*)), whereas the EC+EBW scenario points, EB-CC and EB-HQ, are in the two EC+EBW scans (figures (*b*) and (*c*)).

Even though β_{N} had to be increased to 4.3 to reach target fusion powers, which is above the estimated no-wall β_{N} limit of 3.75 (see table 7), $C_\beta = 0.27$ is still below the suggested 0.5 limit.

Observing the profile data for the four operational points in figure 16, all outputs are relatively similar, except for the EC-LD point, which is characterised by low density (although high density pedestal), high temperature, high $T_{\mathrm{i}}/T_{\mathrm{e}}$, high Z_{eff}, high argon edge density and concentration, and high edge radiation in comparison. The higher ion temperature of the EC-LD point means that a higher xenon content is required for comparable total radiation relative to the other scenarios, which is observed in figure 16(*d*). This in combination with the higher helium ash concentration of EC-LD (see figure 16(*h*)) causes a

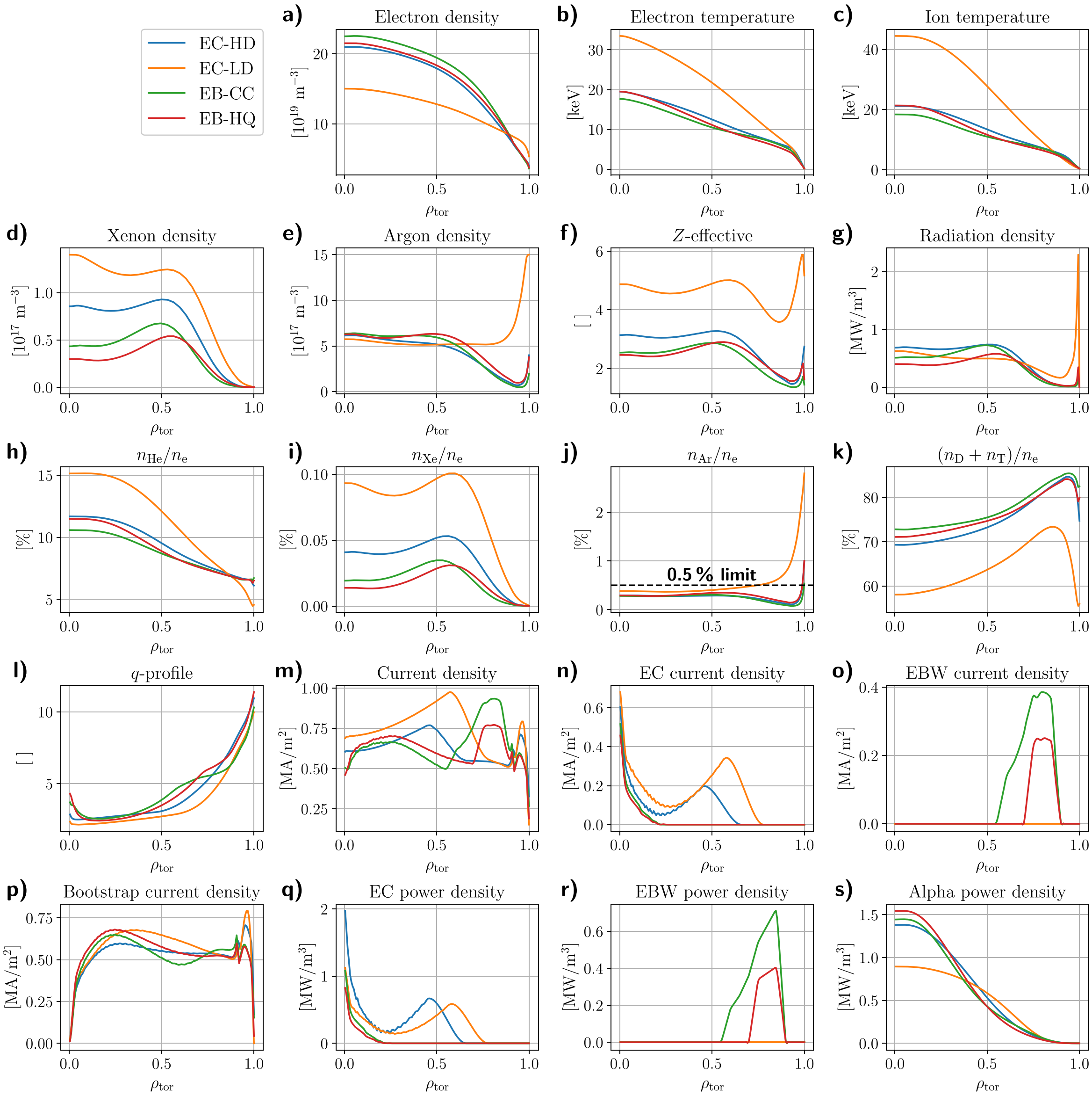

Figure 16. Profile data for candidate operational points.

relatively high degree of dilution (see the lower concentration of D and T in figure 16(*k*)), which is one of the primary reasons why EC-LD under-performs in Q_{sci}. The argon content for all four scenarios is mainly controlled by the density and particle flux boundary conditions set at the separatrix. Their values are set such that the argon concentration is close to, but does not exceed 0.5% in the deep core, which defines the limit of unacceptable dilution by argon. That way, an upper limit of the argon separatrix density can be indicated, to study compatibility with detached plasma conditions using higher fidelity SOL modelling (e.g. SOLPS-ITER). Because of the very different pedestal of the EC-LD case, the neoclassical screening is more efficient than the other scenarios, which is why a higher argon concentration can be set at the separatrix (see figure 16(*j*)).

As seen in table 6, the energy exchange time τ_{ei} is shorter than the energy confinement time, which allows for effective electron–ion temperature equilibration, despite EC, EBW and α-heating primarily heat electrons. The EC-LD points has a relatively long energy exchange time, being roughly half the energy confinement time without radiation correction, which allows electron and ion temperatures farther from equilibration. The fact that $T_i > T_e$ rather than the other way around for EC-LD is due to a combination of $\chi_i \ll \chi_e$ and the overall higher temperatures, which causes a larger ion heating fraction of the alpha heating. The higher edge argon density of EC-LD is a consequence of the difference in neoclassical transport that follows from the different pedestal. The current densities of the two EC points, EC-HD and EC-LD, are flat for $\rho_{tor} \lesssim 0.4$ and $\rho_{tor} \lesssim 0.6$, respectively, compared to the two EC+EBW operational points. The flatness of the current density profile is due to optimisation of the EC current density profile, which is adapted to be complementary to the bootstrap current in such a way that the current density is nearly constant in the domain where EC waves couple to the plasma (compare figures 16(*n*)

Table 6. 0D output for the candidate operational points related to confinement, fuelling and burn-up. $\tau^{*}_{\mathrm{E},100\%}$ is the energy confinement time with 100% of the radiation subtracted, and τ_{ei} is the energy exchange time. All of the listed confinement factors have been evaluated without radiation correction, for consistency.

		EC-HD	EC-LD	EB-CC	EB-HQ
$H_{\mathrm{IPB98(y,2)}}$	[ ]	1.15	1.43	1.03	1.18
H_{ITPA20}	[ ]	1.38	1.61	1.23	1.41
$H_{\mathrm{ITPA20-IL}}$	[ ]	1.04	1.12	0.914	1.07
H_{Petty08}	[ ]	0.646	0.817	0.599	0.701
$H_{\mathrm{NSTX(19)}}$	[ ]	0.306	0.364	0.299	0.343
H_{Kurskiev}	[ ]	0.106	0.152	0.0965	0.111
S_{pel}	$[10^{20}\ \mathrm{s}^{-1}]$	93.5	0.430	102	102
f_{BU}	[%]	6.39	N/A	5.41	5.68
τ_{p}	[s]	11.5	N/A	11.4	11.0
τ_{E}	[s]	1.24	1.67	1.30	1.53
$\tau^{*}_{\mathrm{E},100\%}$	[s]	4.20	5.41	3.98	4.55
τ_{ei}	[s]	0.307	0.834	0.236	0.258

Table 7. Evaluation of the RWM stability limits with MARS-F [36] MHD code for each of the four candidate flat-top points. The destabilisation parameter C_{β} is defined in equation (3).

	EC-HD	EC-LD	EB-CC	EB-HQ
β_{N}	4.50	5.10	3.93	4.30
$\beta_{\mathrm{N}}^{\mathrm{no-wall}}$	3.31	3.92	3.72	3.75
$\beta_{\mathrm{N}}^{\mathrm{ideal-wall}}$	5.53	5.90	5.72	5.76
C_{β}	0.54	0.60	0.11	0.27

and (p)). The resulting q-profile is also flat, sitting at a value far from low-order rationals across most of the minor radius, which is beneficial for avoiding destabilisation of MHD modes such as neoclassical tearing modes.

6. Conclusions

The flat-top operational space of the STEP experiment has been explored using JETTO integrated core plasma model in the initial stages of the development of a net energy output scenario. The modelling focuses on stationary non-inductive flat-top operation points rather than whole pulses. The operational space is explored by performing a series of scans in key plasma parameters, where each scan point is a JETTO simulation that runs until 0D output parameters reach convergence. The output parameters are studied in relation to a set of operational limits that provide guidelines to the viable scenarios. The operational limits relate to e.g. fusion gain, plasma stability and control, detachment access and exhaust management, engineering limitations, and viability of the modelling assumptions. By studying the operational spaces indicated by the scans, a set of candidate flat-top operational points have been developed.

Two main types of scenarios are studied in terms of auxiliary heating and current drive systems. The first type runs with ECsystems only, whereas the second type of scenarios uses a combination of EC and EBW systems. Within the required operational domains, the EC systems only provide absorption in the central part of the plasma ($\rho_{\mathrm{tor}} \lesssim 0.5$), whereas the EBW systems can access off-axis heating and current drive. Even though the auxiliary systems and α-particle heating primarily heat the electrons, ion temperatures comparable to electron temperatures are still expected due to the assumption that $\chi_{\mathrm{e}} \gg \chi_{\mathrm{i}}$[5] (based on experience in ST plasmas [20]). Extrapolation to large size tokamaks also predict improved equilibration of electron and ion temperatures in primarily electron heated plasmas [21].

In order to access a wide range of densities and temperatures in the scans, the Greenwald density fraction, f_{GW}, and the normalised beta, β_{N}, were set-up as inputs to the modelling. Feedback systems acting on the fuelling rate of the plasma and on rescaling of the anomalous diffusivities were applied to access the set targets in f_{GW} and β_{N}, respectively. The confinement enhancement factor relative to the IPB98(y,2) scaling, $H_{\mathrm{IPB98(y,2)}}$, provides an indicator as to the viability of achieving the required confinement, with $H_{\mathrm{IPB98(y,2)}} \gg 1$ indicating an overestimated energy confinement. In mapping out the available operating space, different degrees of confinement have been assumed to account for uncertainties in the expected transport for STEP relevant regimes. A lower confinement assumption tend to require high-density, high auxiliary power operating points, whereas better confinement would allow access to broader density and power parameter regimes.

The expected impurity content, in particular the helium ash concentration, depends largely on the efficiency of the pumping systems. Detachment access requires a high neutral pressure at the divertor, which sets an upper limit to the pumping speed. A lower limit is effectively set by the acceptable dilution by impurities. How large this range of possible pumping speed is, if it exists at all, remains an open question at present. Since JETTO is a core-only plasma model, none of the presented simulations includes a model for pumping. The impact of pumping has effectively been set by the density and particle flux boundary conditions at the last closed flux surface, which have been guided by initial iterations against scrape-off layer and divertor modelling with SOLPS-ITER. In the next stage of flat-top scenario modelling, JETTO will be coupled with EDGE2D/EIRENE to provide more self-consistent modelling of pumping and detachment access together with core plasma conditions at runtime.

Four flat-top points have been suggested from the scoping studies of the operational spaces, two points that were using EC heating systems, and two points that used a combination of EC and EBW heating. The two EC operating points primarily differ by density, with the high-density point having a more restrictive confinement assumption compared to the low-density point. The low-density point has to operate at significantly higher temperatures than the high-density point in order to reach a fusion power of 1.5 GW (the lower recommended limit for STEP). However, it only reaches a scientific fusion energy gain factor Q_{sci} of 9.2, whereas the high-density point

---

[5] We note that first nonlinear gyrokinetic simulations for STEP also find that the heat fluxes $Q_{\mathrm{e}} \gg Q_{\mathrm{i}}$ [18].

predicts operation at $Q_{\mathrm{sci}} = 11.1$. Other performance issues of the low-density point that have been demonstrated is a higher risk of uncontrollable growth of RWMs and a high plasma current $I_{\mathrm{p}} > 25$ MA, which might cause unacceptable levels of damage to the tokamak during disruption events.

The two EC+EBW scenario points mainly differ by the auxiliary power, with the high power case using $P_{\mathrm{EC}} = 9.0$ MW and $P_{\mathrm{EBW}} = 120.0$ MW, compared to $P_{\mathrm{EC}} = 6.3$ MW and $P_{\mathrm{EBW}} = 48.2$ MW for the low power case. The high-power EC+EBW scenario point has a much lower confinement factor than both of the EC points, with $H^{*}_{98} = 1.19$ (radiation corrected IPB98(y,2) confinement factor, see details in section 2.6), whereas the low-power point has a similar confinement factor as the one estimated for the high-density EC point ($H^{*}_{98} = 1.36$ and $H^{*}_{98} = 1.35$, respectively), making the EC+EBW scenario in general more viable than the EC scenario in terms of confinement assumptions. The low-power EC+EBW point also has relatively high $Q_{\mathrm{sci}} = 29.1$, making it an attractive point for the development of commercial fusion reactors. No operating point has been found with $H^{*}_{98} < 1.19$ so far.

The main caveat of the EC+EBW scenario in general is that available EBW heating and current drive models have limited experimental validation, making the assumption of a high EBW current drive efficiency ($I_{\mathrm{EBW}}/P_{\mathrm{EBW}} > 30\,\mathrm{kA\,MW^{-1}}$) less certain. On the other hand, a scenario with only EC heating and current drive requires more optimistic confinement time assumptions in order to provide sufficient fusion gain. Since transport models also lack experimental validation for STEP relevant regimes, considerable uncertainty remains in the viability of both scenarios. However, it should be noted that one of the most important products of the presented work is not necessarily the specific operating points that have been derived, but rather the development of a robust methodology for generating designs of non-inductive, burning plasmas. On a related note, the ST MAST-U will soon undergo significant enhancements, including the installation of an EBW system and a second neutral beam injector box. With these upgrades, MAST-U will be able to provide important experimental data that will improve our understanding of EBW heating and current drive and of transport in more STEP relevant plasmas.

Acknowledgments

This work has been funded by STEP, a UKAEA programme to design and build a prototype fusion energy plant and a path to commercial fusion. To obtain further information on the data and models underlying this paper please contact PublicationsManager@ukaea.uk.

Appendix. Particle confinement for the EC-LD operational point

As stated in section 5, the low-density operational point with EC heating and current drive only (labelled as EC-LD) demonstrated a particle confinement time $\tau_{\mathrm{p}} = V\langle n_{\mathrm{e}}\rangle/S_{\mathrm{pel}}$ of the order 1000 s, and a burn-up fraction $f_{\mathrm{BU}} = S_{\alpha}/S_{\mathrm{pel}}$ of the order 1000%. The pellet injection rate is naturally lower in a low-density scenario compared against an equivalent higher density scenario. However, for EC-LD, S_{pel} is a factor ~200 smaller than other candidate flat-top operational points, as seen in table 6, which is why τ_{p} and f_{BU} blows up for this case. The heat confinement time is also higher for EC-LD than any other operational point, but all four points are still within the same order of magnitude, with τ_{E} between 1 and 2 s (without radiation correction). Thus, closer attention needs to be given specifically to the particle confinement for this operational point.

Figures A1(*a*) and (*b*) present the predicted deuterium diffusivity in the edge/pedestal and axis regions, respectively, for all four operational points. Corresponding tritium diffusivity profiles are qualitatively the same (there is an isotope dependency in the neoclassical diffusivity). The EC-LD point stands out, having a higher edge particle diffusivity, which would normally indicate a comparably poor confinement. However, the empirical pinch term that was added (see equation (12)) is proportional to the diffusivity, meaning that it counteracts the diffusivity to improve confinement. This term is consequently larger for EC-LD, as seen in figures A1(*c*) and (*d*).

Repeating the EC-LD scenario with the pinch term disabled generates the cyan curves in figure A2. the most notable difference is that the density peaking is significantly reduced. The diffusivity is reduced on-axis, as seen in figure A2(*j*). However, with the dropping of the inward pinch term, the particle confinement is reduced on average, leading to the reduced density peaking. The Z_{eff} profile has dropped for $\rho_{\mathrm{tor}} \lesssim 0.6$ (see figure A2(*h*)), indicating a reduction of impurity ion confinement. The reduced on-axis density also increases the EC current drive (see figure A2(*f*)), which is proportional to $T_{\mathrm{e}}/n_{\mathrm{e}}$ (see equation (16)). As a result, the q on-axis drops significantly (see figure A2(*d*)), which can potentially trigger MHD instabilities such as NTMs and sawteeth (see section 2.4). The ECCD will need to be re-optimised to make this a viable scenario. It is likely that removal of the empirical pinch term has significant impacts on the particle confinement and the density peaking also for the three other operational points. In later iterations of the STEP concept design, the empirical pinch will have to be reassessed.

Table A1 summarises 0D outputs from the simulations with and without the empirical pinch term. It can be seen that the removal of the pinch term made both the burn-up fraction and the particle confinement time to approach physical values, with $f_{\mathrm{BU}} = 29.6\%$, and $\tau_{\mathrm{p}} = 44.1$ s. The values are still high compared to the other operational points, which have f_{BU} between 5.4 and 6.4%, and τ_{p} between 11.0 and 11.5 s. The pellet injection rate went from being a factor ~200 smaller to a factor 5.3–5.8 smaller. There is a slightly reduced fusion power performance due to the reduced density peaking. The reduced impurity confinement caused a reduction of impurity radiation by 26%, which in turn increased $P_{\mathrm{sep}}/R_{\mathrm{geo}}$ from 40.1 to 59.2 $\mathrm{MW\,m^{-1}}$. The confinement factor also decreased slightly. However, increasing the impurity seeding in order to raise the radiation fraction and lower $P_{\mathrm{sep}}/R_{\mathrm{geo}}$ is likely to increase the confinement factor again, as indicated by figure 14(*f*).

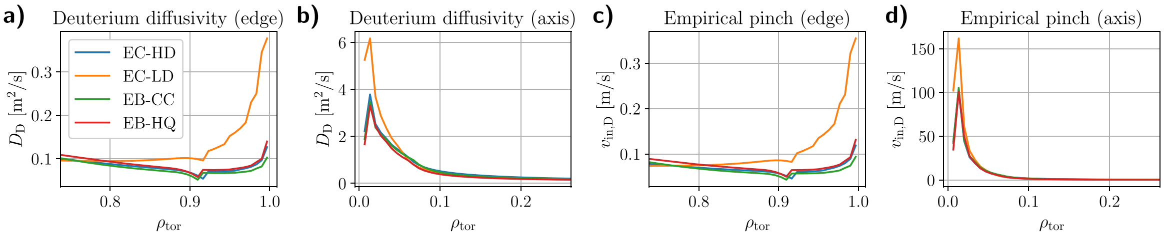

Figure A1. Particle transport data for the four candidate operational points, zoomed into the edge and axis regions separately. (*a*) and (*b*) Neoclassical + anomalous deuterium diffusivity. (*c*) and (*d*) Empirical inward pinch for deuterium, defined by equation (12).

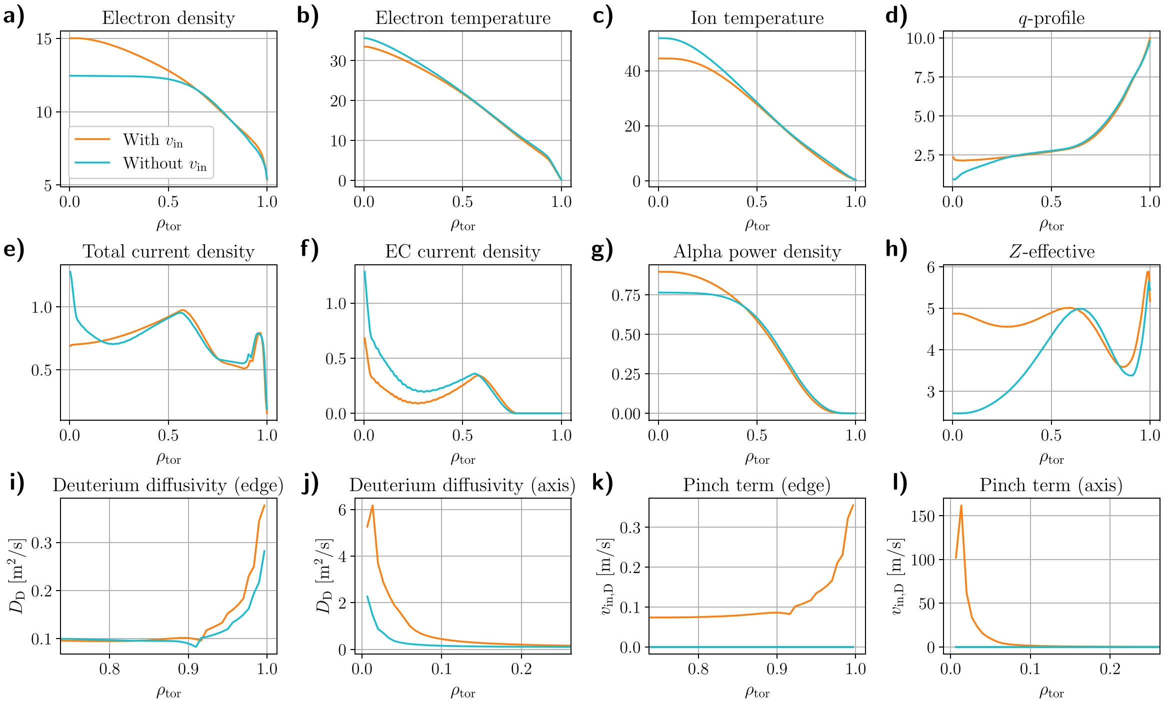

Figure A2. Profile data for the EC-LD flat-top operational point, both with and without the empirical pinch term of equation (12).

Table A1. Summary of 0D outputs from the EC-LD operational points with and without the empirical pinch term.

		With v_{in}	Without v_{in}
P_{fus}	[GW]	1.51	1.48
Q_{sci}	[ ]	9.22	9.03
I_{p}	[MA]	25.1	25.0
$P_{\text{sep}}/R_{\text{geo}}$	[MW m^{-1}]	40.1	59.2
H^{*}_{98}	[ ]	1.62	1.59
P_{EC}	[MW]	160	160
P_{rad}	[MW]	321	237
$P_{\text{sep}} - P_{\text{L-H}}$	[MW]	110	181
$\langle n_{\text{e}} \rangle$	[10^{19} m^{-3}]	11.6	11.0
$\langle n_{\text{e}} \rangle_{\text{line}}/n_{\text{GW}}$	[%]	61.2	56.6
$\langle T_{\text{e}} \rangle$	[keV]	18.1	18.6
$\langle T_{\text{i}} \rangle/\langle T_{\text{e}} \rangle$	[ ]	1.24	1.28
$I_{\text{BS}}/I_{\text{p}}$	[%]	81.1	76.4
I_{EC}	[MA]	4.22	5.40
$I_{\text{EC}}/P_{\text{EC}}$	[kA MW^{-1}]	26.4	33.7
β_{N}	[%]	5.10	5.10
β_{tor}	[%]	20.0	19.9
B_{axis}	[T]	2.46	2.49
l_{i}	[ ]	0.529	0.511
$l_{\text{i}}(3)$	[ ]	0.296	0.286
q_{min}	[ ]	2.15	0.919
q_{95}	[ ]	7.93	7.94
Z_{eff}	[ ]	4.58	3.97
S_{pel}	[10^{20} s^{-1}]	0.430	17.7
f_{BU}	[%]	1250	29.6
τ_{p}	[s]	1930	44.1
τ_{E}	[s]	1.67	1.66
$\tau^{*}_{\text{E},100\%}$	[s]	5.41	3.44
τ_{ei}	[s]	0.834	0.927

There is a decrease of the Greenwald fraction from 61.2 to 56.6%. This is because the target for the fuelling feedback was set to a line-averaged electron density of 11.2×10^{19} m^{-3}. The EC-LD case without the empirical pinch term could not reach this target (it finished at $\langle n_{\text{e}} \rangle_{\text{line}} = 12.2 \times 10^{19}$ m^{-3}), since the fuelling rate could not be reduced much further. On the other hand, the case without the pinch term succeeded to reach the target density. Even though the ECCD increased by nearly 30%, the total current stayed more or less the same, since the reduced density peaking caused a reduction of the bootstrap current.

ORCID iDs

E. Tholerus https://orcid.org/0000-0002-3262-1958
F.J. Casson https://orcid.org/0000-0001-5371-5876
S.P. Marsden https://orcid.org/0009-0005-1175-7329
T. Wilson https://orcid.org/0009-0001-4343-834X
D. Brunetti https://orcid.org/0000-0001-8650-3271
P. Fox https://orcid.org/0009-0004-2993-7611
S.J. Freethy https://orcid.org/0000-0003-4535-565X
S.S. Henderson https://orcid.org/0000-0002-8886-1256
A. Hudoba https://orcid.org/0000-0002-8197-7977
K.K. Kirov https://orcid.org/0000-0001-8104-4782
F. Koechl https://orcid.org/0000-0001-9706-6855
H. Meyer https://orcid.org/0000-0002-5565-1199
S.I. Muldrew https://orcid.org/0000-0001-5940-3523
B.S. Patel https://orcid.org/0000-0003-0121-1187
C.M. Roach https://orcid.org/0000-0001-5856-0287
S. Saarelma https://orcid.org/0000-0002-6838-2194
G. Xia https://orcid.org/0009-0009-4236-077X

References

[1] Donné A.J.H. 2019 *Phil. Trans. R. Soc.* A **377** 20170432
[2] Wilson H.R., Chapman I., Denton T., Morris W., Patel B., Voss G. and Waldon C. (the STEP team) 2020 STEP-on the pathway to fusion commercialization *Commercialising Fusion Energy* (IOP Publishing) ch 8
[3] Meyer H for the STEP Plasma, Control and Heating & Current Drive Team and Contributors 2022 The physics of the preferred plasma scenario for STEP *Proc. 48th EPS Conf. on Plasma Physics* (*Maastricht, Netherlands*, *27 June–1 July 2022*) (available at: https://indico.fusenet.eu/event/28/contributions/302/attachments/316/991/EPS2022_paper_HMeyer_v3.pdf)
[4] Muldrew S.I. *et al* 2024 *Fusion Eng. Des.* **201** 114238
[5] Menard J.E., Jardin S.C., Kaye S.M., Kessel C.E. and Manickam J. 1997 *Nucl. Fusion* **37** 595
[6] Wilson H.R. *et al* 2004 *Nucl. Fusion* **44** 917
[7] Andrade M.C.R. and Ludwig G.O. 2008 *Plasma Phys. Control. Fusion* **50** 065001
[8] ITER Physics Expert Group on Confinement and Transport, ITER Physics Expert Group on Confinement Modelling and Database and ITER Physics Basis Editors 1999 *Nucl. Fusion* **39** 2175
[9] Costley A.E., Hugill J. and Buxton P.F. 2015 *Nucl. Fusion* **55** 033001
[10] Buxton P.F., Connor J.W., Costley A.E., Gryaznevich M.P. and McNamara S. 2019 *Plasma Phys. Control. Fusion* **61** 035006
[11] Meyer H. (the STEP Plasma Team) 2024 *Phil. Trans. R. Soc.* A **382** 20230406
[12] Menard J.E. *et al* 2011 *Nucl. Fusion* **51** 103014
[13] Patel B.S. 2021 Confinement physics for a steady state net electric burning spherical tokamak *PhD Thesis* University of York
[14] Henderson S.S. *et al* 2024 *Nucl. Fusion* **64** 066006
[15] Lux H., Kemp R., Fable E. and Wenninger R. 2016 *Plasma Phys. Control. Fusion* **58** 075001
[16] Kennedy D., Giacomin M., Casson F.J., Dickinson D., Hornsby W.A., Patel B.S. and Roach C. 2023 *Nucl. Fusion* **63** 126061
[17] Patel B.S., Dickinson D., Roach C.M. and Wilson H.R. 2022 *Nucl. Fusion* **62** 016009
[18] Giacomin M., Kennedy D., Casson F.J., Ajay C.J., Dickinson D., Patel B.S. and Roach C.M. 2024 *Plasma Phys. Control. Fusion* **66** 055010
[19] Giacomin M., Dickinson D., Dorland W., Mandell N.R., Bokshi A., Casson F.J., Dudding H.G., Kennedy D., Patel B.S. and Roach C.M. 2024 A quasi-linear model of electromagnetic turbulent transport and its application to flux driven transport predictions for STEP *J. Plasma Phys.* accepted
[20] Kaye S.M., Connor J.W. and Roach C.M. 2021 *Plasma Phys. Control. Fusion* **63** 123001
[21] Angioni C., Bonanomi N., Fable E., Schneider P.A., Tardini G., Luda T. and Satebler G.M. (the ASDEX Upgrade Team) 2023 *Nucl. Fusion* **63** 056005
[22] Hudoba A., Newton S., Voss G., Cunningham G. and Henderson S. 2023 *Nucl. Mater. Energy* **35** 101410

[23] Hudoba A., Cunningham G. and Bakes S. (STEP team) 2023 *Fusion Eng. Des.* **191** 113704

[24] Hudoba A., Bakes S., Cunningham G., Henderson S., Eriksson F., Marsden S. and Wilson T. (the STEP Team) 2024 *Nucl. Fusion* **64** 086055

[25] Osawa R.T., Moulton D., Newton S.L., Henderson S.S., Lipschultz B. and Hudoba A. 2023 *Nucl. Fusion* **63** 076032

[26] Kallenbach A., Bernert M., Dux R., Reimold F. and Wischmeier M. (ASDEX Upgrade Team) 2016 *Plasma Phys. Control. Fusion* **58** 045013

[27] Henderson S.S. *et al* 2023 *Nucl. Fusion* **63** 086024

[28] Muldrew S.I., Lux H., Cunningham G., Hender T.C., Kahn S., Knight P.J., Patel B., Voss G.M. and Wilson H.R. 2020 *Fusion Eng. Des.* **154** 111530

[29] Kovari M., Kemp R., Lux H., Knight P., Morris J. and Ward D.J. 2014 *Fusion Eng. Des.* **89** 3054

[30] Kovari M., Fox F., Harrington C., Kembleton R., Knight P., Lux H. and Morris J. 2016 *Fusion Eng. Des.* **104** 9

[31] Cenacchi G. and Taroni A. 1988 JETTO: a free boundary plasma transport code JET-IR(88)03 (available at: https://inis.iaea.org/collection/NCLCollectionStore/_Public/19/097/19097143.pdf)

[32] Mikhailovskii A.B., Huysmans G.T.A., Kerner W.O.K. and Sharapov S.E. 1997 *Plasma Phys. Rep.* **23** 844

[33] Huysmans G.T.A., Sharapov S.E., Mikhailovskii A.B. and Kerner W. 2001 *Phys. Plasmas* **8** 4292

[34] Sharapov S.E., Mikhailovskii A.B. and Huysmans G.T.A. 2004 *Phys. Plasmas* **11** 2286

[35] Chapman I.T., Sharapov S.E., Huysmans G.T.A. and Mikhailovskii A.B. 2006 *Phys. Plasmas* **13** 062511

[36] Liu Y.Q., Bondeson A., Fransson C.M., Lennartson B. and Breitholtz C. 2000 *Phys. Plasmas* **7** 3681

[37] Cunningham G. 2013 *Fusion Eng. Des.* **88** 3238

[38] Farina D. 2007 *Fusion Sci. Technol.* **52** 154

[39] Smirnov A.P., Harvey R.W. and Prater R. 1995 *Bull. Am. Phys. Soc.* **40** 1837

[40] Harvey R.W. and McCoy M.G. 1992 The CQL3D Fokker-Planck Code GA-A20978 General Atomics (available at: https://www.compxco.com/cql3d_manual.pdf)

[41] Saarelma S., Frassinetti L., Bilkova P., Challis C.D., Chankin A., Fridström R., Garzotti L., Horvath L. and Maggi C.F. (JET Contributors) 2019 *Phys. Plasmas* **26** 072501

[42] Kotschenreuther M., Gewoldt G. and Tang W.M. 1995 *Comput. Phys. Commun.* **88** 128

[43] Candy J., Belli E.A. and Bravenec R.V. 2016 *J. Comput. Phys.* **324** 73

[44] Jenko F., Dorland W., Kotschenreuther M. and Rogers B.N. 2000 *Phys. Plasmas* **7** 1904

[45] Wiesen S. *et al* 2015 *J. Nucl. Mater.* **463** 480

[46] Menard J.E. *et al* 2016 *Nucl. Fusion* **56** 106023

[47] Peeters A.G. 2000 *Plasma Phys. Control. Fusion* **42** B231

[48] Xia G., Liu Y., Hender T., McClements K., Trier E. and Tholerus E. 2023 *Nucl. Fusion* **63** 026021

[49] Taylor G., Efthimion P.C., Kessel C.E., Harvey R.W., Smirnov A.P., Ershov N.M., Carter M.D. and Forest C.B. 2004 *Phys. Plasmas* **11** 4733

[50] Urban J., Decker J., Peysson Y., Preinhaelter J., Shevchenko V., Taylor G., Vahala L. and Vahala G. 2011 *Nucl. Fusion* **51** 083050

[51] Freethy S.J. *et al* 2023 The STEP microwave heating and current drive system *Nucl. Fusion* submitted

[52] Preinhaelter J. and Kopecký V. 1973 *J. Plasma Phys.* **10** 1

[53] Challis C.D. *et al* 2002 *Plasma Phys. Control. Fusion* **44** 1031

[54] Yu Q. 2022 *Nucl. Fusion* **62** 126024

[55] Fredrickson E., Bell M., Budny R.V. and Synakowski E. 2000 *Phys. Plasmas* **7** 4112

[56] Mahajan S.M. and Hazeltine R.D. 1982 *Nucl. Fusion* **22** 1191

[57] Breizman B.N., Berk H.L., Pekker M.S., Pinches S.D. and Sharapov S.E. 2003 *Phys. Plasmas* **10** 3649

[58] Sharapov S.E. *et al* 2002 *Phys. Plasmas* **9** 2027

[59] Helander P. 2000 *Phys. Plasmas* **7** 2878

[60] Mercier C. 1978 *Proc. 7th IAEA Conf. on Plasma Physics and Controlled Nuclear Fusion Research* (*Innsbruck, Austria, 23–30 August 1978*) vol 1 p 701 (available at: https://www.iaea.org/publications/3309/plasma-physics-and-controlled-nuclear-fusion-research-1978-proceedings-of-an-international-conference-innsbruck-23-30-aug-1978)

[61] La Haye R.J., Buttery R.J., Gerhardt S.P., Sabbagh S.A. and Brennan D.P. 2012 *Phys. Plasmas* **19** 062506

[62] Manickam J., Pomphrey N. and Todd A.M.M. 1987 *Nucl. Fusion* **27** 1461

[63] Marsden S.P., Casson F.J., Freethy S., Wilson T., Patel B. and Tholerus E. 2022 Using genetic algorithms to optimise current drive in STEP *Proc. 48th EPS Conf. on Plasma Physics* (*Maastricht, Netherlands, 27 June–1 July, 2022*) (available at: https://indico.fusenet.eu/event/28/contributions/168/attachments/182/1230/proceedings-v2.pdf)

[64] Brown T., Marsden S., Gopakumar V., Terenin A., Ge H. and Casson F.J. 2024 *IEEE Trans. Plasma Sci.* 1–6

[65] Ham C.J., Gimblett C.G. and Hastie R.J. 2009 *Plasma Phys. Control. Fusion* **51** 115010

[66] Gerhardt S.P., Andre R. and Menard J.E. 2012 *Nucl. Fusion* **52** 083020

[67] Rosenbluth M.N. and Hinton F.L. 1996 *Nucl. Fusion* **36** 55

[68] Snicker A., Asunta O., Ylitie H., Kurki-Suonio T., Schneider M. and Pinches S. 2015 *Nucl. Fusion* **55** 063023

[69] Lang P.T. *et al* 2014 *Nucl. Fusion* **54** 083009

[70] Luce T.C., Humphreys D.A., Jackson G.L. and Solomon W.M. 2014 *Nucl. Fusion* **54** 093005

[71] Staebler G.M., Kinsey J.E. and Waltz R.E. 2005 *Phys. Plasmas* **12** 102508

[72] Bourdelle C., Garbet X., Imbeaux F., Casati A., Dubuit N. and Parisot T. 2007 *Phys. Plasmas* **14** 112501

[73] Petty C.C. 2008 *Phys. Plasmas* **15** 080501

[74] Verdoolaege G. *et al* 2021 *Nucl. Fusion* **61** 076006

[75] Valovič M. *et al* 2009 *Nucl. Fusion* **49** 075016

[76] Valovič M., Meyer H., Akers R., Brickley C., Conway N.J., Cunningham G., Kirk A., Lloyd B., Patel A. and Taylor D. 2005 *Nucl. Fusion* **45** 942

[77] Valovič M. *et al* 2019 *Nucl. Fusion* **59** 106047

[78] Stork D. *et al* 2005 *Nucl. Fusion* **45** S181

[79] Zastrow K.-D. *et al* 2004 *Plasma Phys. Control. Fusion* **46** B255

[80] Angioni C., Fable E., Greenwald M., Maslov M., Peeters A.G., Takenaga H. and Weisen H. 2009 *Plasma Phys. Control. Fusion* **51** 124017

[81] Henderson S.S. *et al* 2024 *Nucl. Fusion* **64** 066006

[82] Eich T. *et al* 2013 *Nucl. Fusion* **53** 093031

[83] Kallenbach A., Dux R., Henderson S.S., Tantos C., Behnert M., Day C., McDermott R.M., Rohde V. and Zito A (the ASDEX Upgrade Team) 2024 *Nucl. Fusion* **64** 056003

[84] Dux R., Loarte A., Fable E. and Kukushkin A. 2014 *Plasma Phys. Control. Fusion* **56** 124003

[85] Field A.R. *et al* 2023 *Nucl. Fusion* **63** 016028

[86] SimDB reference: `b3be18d8b91711ed91b58fb75cac1b85` Alias: `smars/jetto/step/88888/mar0123/seq-1`

[87] SimDB reference: `056300b0b6a011edbc0cd3cc3172bccc` Alias: `twilson/jetto/step/88888/feb2723/seq-1`

[88] Simonini R., Corrigan G., Radford G., Spence J. and Taroni A. 1994 *Contrib. Plasma Phys.* **34** 368

[89] Reiter D., Baelmans M. and Börner P. 2005 *Fusion Sci. Technol.* **47** 172

[90] Romanelli M. *et al* 2014 *Plasma Fusion Res.* **9** 3403023

[91] Roach C.M. *et al* 2009 *Plasma Phys. Control. Fusion* **51** 124020

[92] Houlberg W.A., Shaing K.C., Hirshman S.P. and Zarnstorff M.C. 1997 *Phys. Plasmas* **4** 3230

[93] Erba M., Cherubini A., Parail V.V., Springmann E. and Taroni A. 1997 *Plasma Phys. Control. Fusion* **39** 261

[94] Pégourié B., Waller V., Nehme H., Garzotti L. and Géraud A. 2007 *Nucl. Fusion* **47** 44

[95] Snyder P.B., Groebner R.J., Leonard A.W., Osborne T.H. and Wilson H.R. 2009 *Phys. Plasmas* **16** 056118

[96] Martin Y.R. and Takizuka T. (the ITPA CDBM H-mode Threshold Database Working Group) 2008 *J. Phys.: Conf. Ser.* **123** 012033

[97] Righi E. *et al* 1999 *Nucl. Fusion* **39** 309

[98] Mikkelsen D.R. and Singer C.E. 2017 *Nucl. Technol. Fusion* **4** 237

[99] Estrada-Mila C., Candy J. and Waltz R.E. 2006 *Phys. Plasmas* **13** 112303

[100] Luce T.C., Lin-Liu Y.R., Harvey R.W., Giruzzi G., Politzer P.A., Rice B.W., Lohr J.M., Petty C.C. and Prater R. 1999 *Phys. Rev. Lett.* **83** 4550

[101] Lauro-Taroni L., Alper B., Giannella R., Lawson K., Marcus F., Mattioli M., Smeulders P. and von Hellermann M. 1994 *21st EPS Conf. on Controlled Fusion and Plasma Physics* (*Montpellier, France, 27 June–1 July, 1994*) vol 18B p 102 (available at: http://libero.ipp.mpg.de/libero/PDF/EPS_21_Vol1_1994.pdf)

[102] Kurskiev G.S. *et al* 2022 *Nucl. Fusion* **62** 016011

[103] SimDB reference: `774985686d9e11ee834fc9a93c9c1edd`
Alias: `smars/jetto/step/88888/oct1223/seq-1`

[104] SimDB reference: `5aec0d50105111ee82ecb9a153e8f3e0`
Alias: `smars/jetto/step/88888/jun2123/seq-2`

[105] SimDB reference: `d9d7029a053f11ee99fc6f3cc269b851`
Alias: `twilson/jetto/step/88888/may3123/seq-2`

[106] SimDB reference: `76a1e51a14cf11eeba0e7fdeaaba66cd`
Alias: `twilson/jetto/step/88888/jun2623/seq-2`